PLANETARY INSTRUMENT DEFINITION AND DEVELOPMENT PROGRAM:

"MINIATURE MONOCHROMATIC IMAGER"

FINAL TECHNICAL REPORT FOR NASA GRANT NASW-4245

A. L. Broadfoot

Principal Investigator

Lunar and Planetary Laboratory

University of Arizona

901 Gould-Simpson Building

Tucson, Arizona 85721

August 12, 1991

FINAL TECHNICAL REPORT

NASA Contract NASW-4245

"MINIATURE MONOCHROMATIC IMAGERS"

By A. L. Broadfoot

The miniature monochromatic imager (MMI) development work was very successful. That work became the basis for the preparation of several instruments which have been built and flown on the shuttle as well as being used in ground-based experiments. We have used the results of our development work in several proposals to NASA Planetary (Cassini) and NASA Space Physics Division (SPD) with respect to plasmasphere imaging.

The work has been written up in two papers (attached) which have been accepted for publication as companion papers in Applied Optics. The first paper covers the philosophy and design considerations, "Applications of the ICCD to Airglow and Auroral Measurements" by Broadfoot and Sandel. The second paper, "A Panchromatic Spectrograph with Supporting Monochromatic Imagers", Broadfoot et al., describes the first real application of the MMI. It is noteworthy that the support imagers included twelve different images through various bandpass filters.

We now have data from the instrument described in the second paper which was flown on STS-39 and some images have been included as a demonstration of the capability.

The series of five images, Plate #1, were taken with the AIS on the STS-39 as the spacecraft moved from day time across the terminator into the night side of the planet. Early images were saturated because we had little communication with the spacecraft and no exposure control. The first image shows the earth's terminator and limb in the background. The second image shows the bright limb which is repeated in successive images. The streak across #3 is a sunlight dust particle. The important feature is the position of the spectrograph field of view with respect to the limb. The imager field of view was 21° x 19° with a resolution of 0.15° per pixel although we normally recorded summing 2 x 2 pixels because of our data rate. In these limb images the height resolution at the limb would be ~10 km.

The second series of images, Plate #2, shows the field of view moving up from viewing the night side of the earth through the limb into the atmosphere above the earth. In this case the slit is superimposed on

the imaging frame. The Wide IR channel had a field of view 21° wide while the slit was 2° long and about 0.2° wide. At the bottom is a narrow IR image shuttered simultaneously with the Wide IR. In the case of the narrow IR the field of view is 2.3° x 2.0° and just accommodates the slit. This is a very useful capability for data analysis. The scale at the limb, 1800 km away, is about 1 km per pixel (2 x 2) or the image height in the atmosphere at the limb is 64 km from the bottom to top of the narrow IR image.

At these miniature scales the optical quality requirements can be reduced. The lenses we use have rather short focal lengths, 5-10mm. At these scales our pixels are relatively large and it is quite easy to get a reasonable resolution even though the aberrations are strong. The throughput is high also. The AIS imagers are about f/2 because of the simplicity of the optics involved.

As mentioned above, we are actively using the MMI techniques developed with the help of the PIDDP program. In the near future we will fly a Hitchhiker payload with fifteen imagers and we anticipate a second flight of the AIS instrument with a similar complement. We also have six imager sets in our instruments on the ground-based telescopes at AMOS/Haleakela. The more we work with these applications the more easily we can adapt to other experimental opportunities.

Finally, we have included an image of the shuttle tail section, Plate 3. Although the spatial resolution is poor for examining the shuttle edges, the important signature, the shuttle glow, is quite apparent on the left side of the tail section. The MMI investigation does demonstrate an approach which allows significant types of spatial information to be recorded with minimum data and instrumental impact. We also have the important feature of simultaneous shuttering of all detectors.

We have several different types of support imagers now. We are developing a replacement for the flexible fiber optic bundles. The enclosed photographs (Figures 1 - 7) show a solid coupler which couples six images on a proximity focused intensifier to one CCD.

CONCLUSIONS:

Our conclusions are illustrated by the applications we have cited. Our MMI techniques have been successfully developed with the aid of the Planetary Instrument Definition and Development Program and are being used in many applications at this time. These techniques have been written up and are being published.
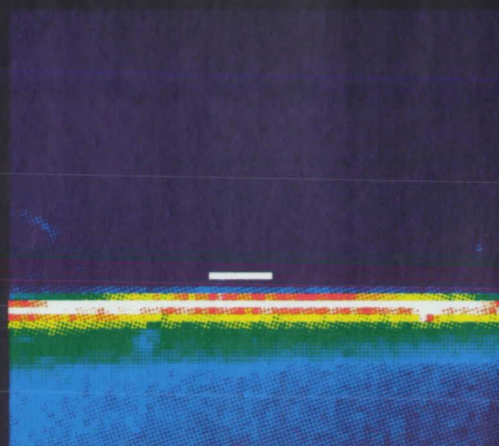
PLATE 1

NIE4/Earthlimb Images, Exposure = 10 sec.
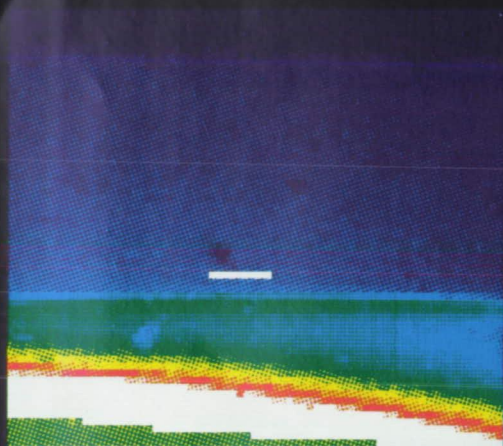
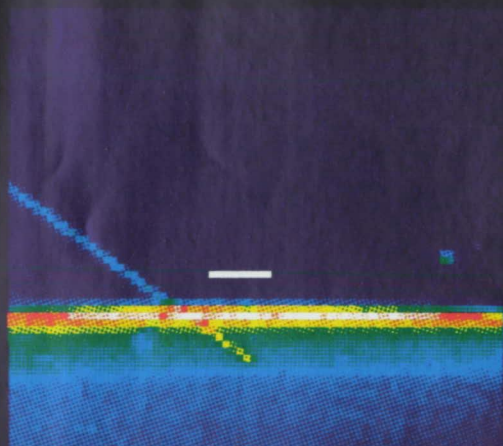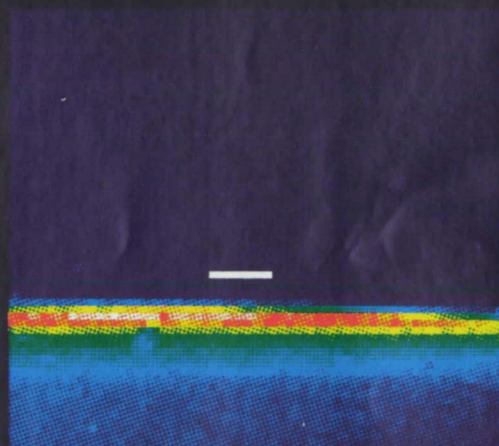6/21:08:19.17 WIR

6/21:09:54.30 WIR

6/21:10:57.55 WIR

6/21:15:49.62 WIR

6/21:20:37.34 WIR

PLATE 2
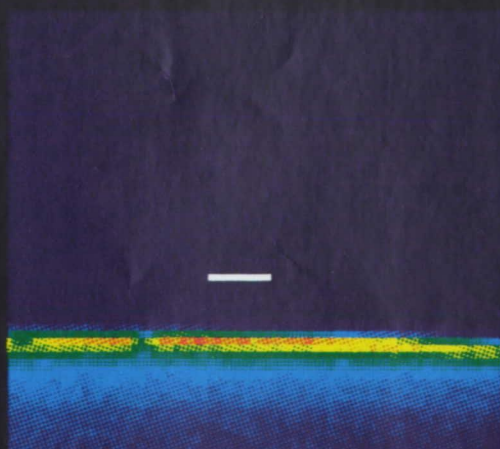
RMS1/NO Earthlimb Images, Exposure = 10 sec.
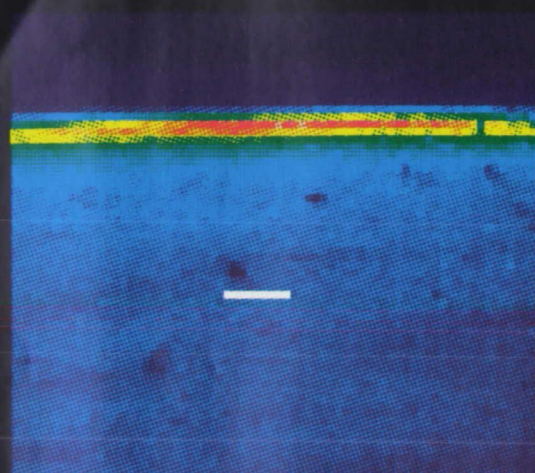
5/04:57:51.25   WIR
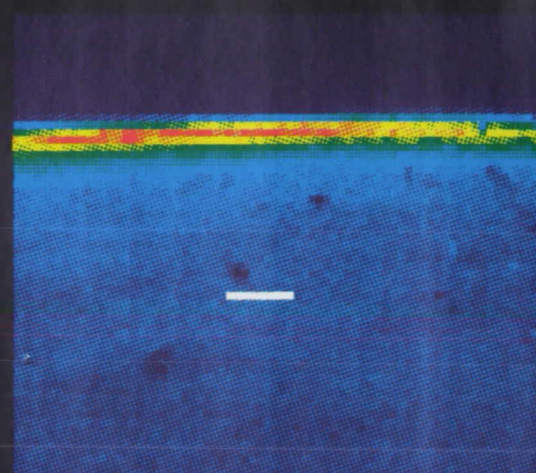
5/04:58:54.50   WIR
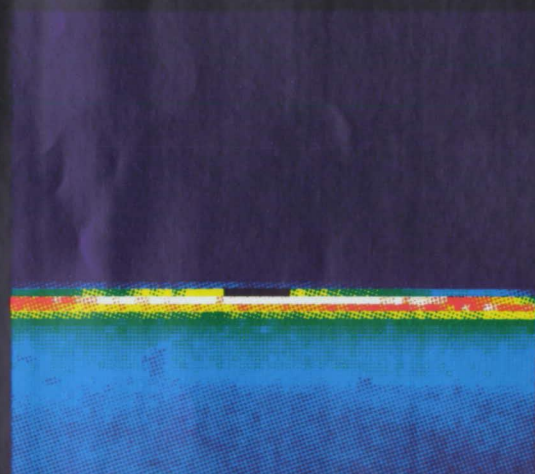
5/05:03:48.66   WIR
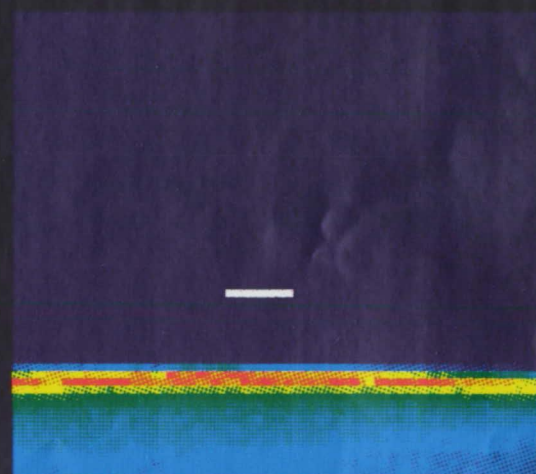
5/05:08:39.05   WIR

5/05:03:48.66   NIR

PLATE 3
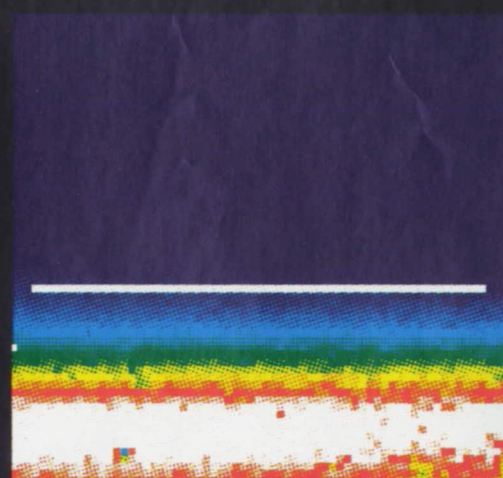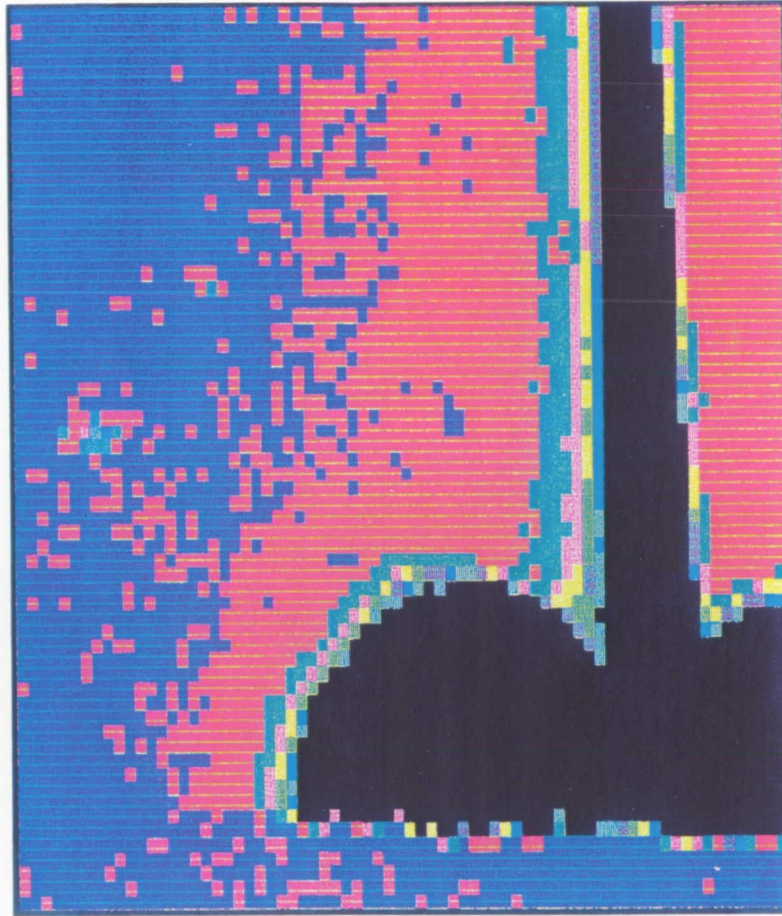
AIS Data Sample   MET 05/25:30

The unprocessed false color image was obtained by the AIS wide angle IR imager. The ram side of the tail section and OMS pod show excess emission which is shuttle glow. The spectrographs and narrow angle imagers, 2° FOV, are bore-sighted in the center of this 20° field of view.
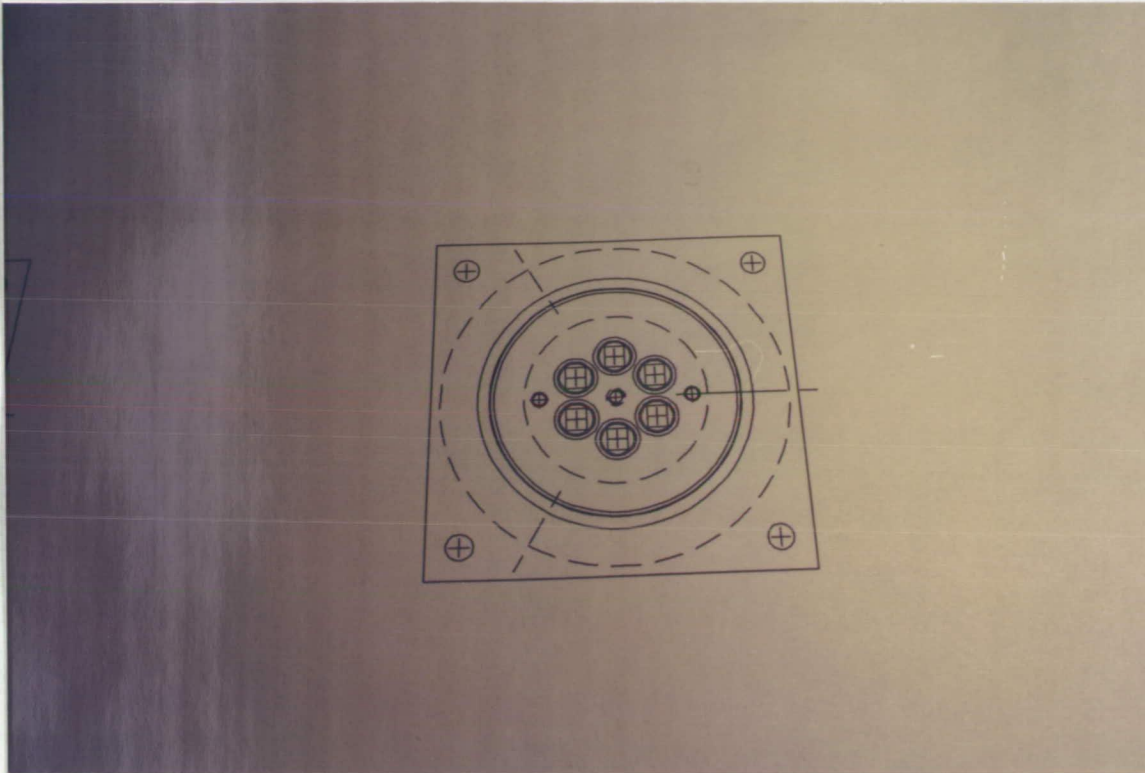
Figure 1. This photograph shows a drawing of the positions of 6 optical axes on an 18 mm image intensifier.
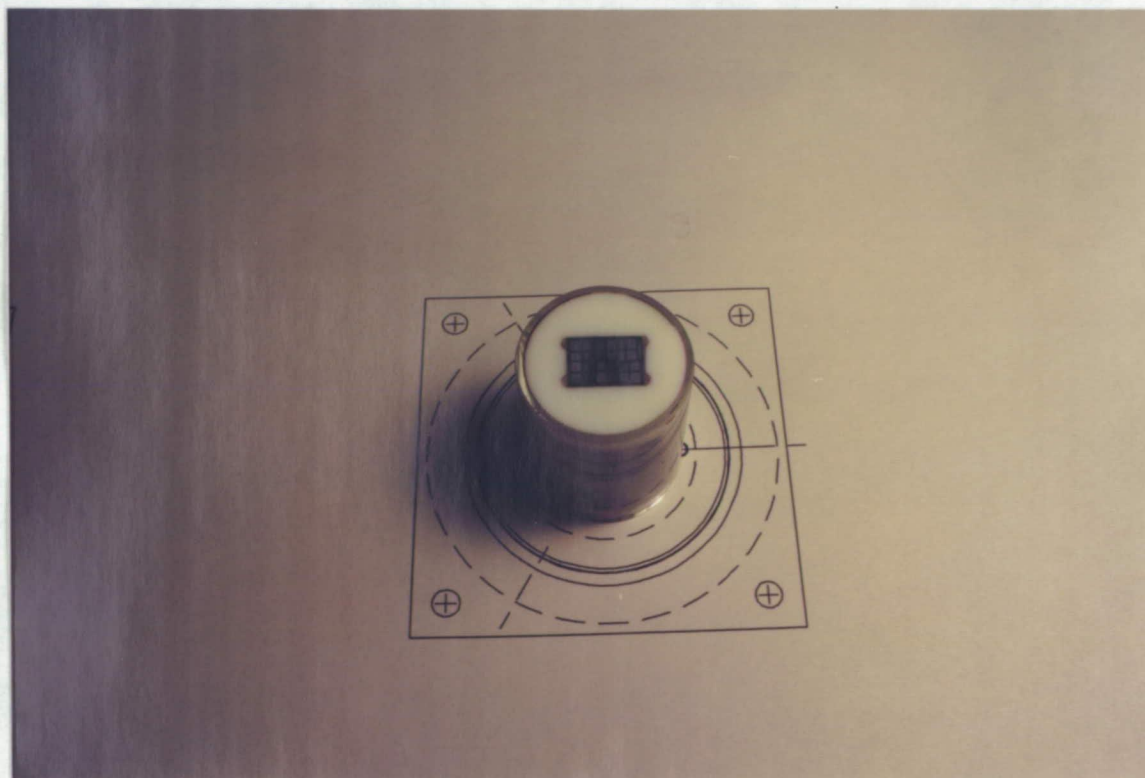
Figure 2. In this photo the fiberoptic coupler is placed on the drawing Figure 1. The crosses from the centers of the circular intensifier pattern appear in the rectangular format which is to couple to the image half of a frame transfer CCD.
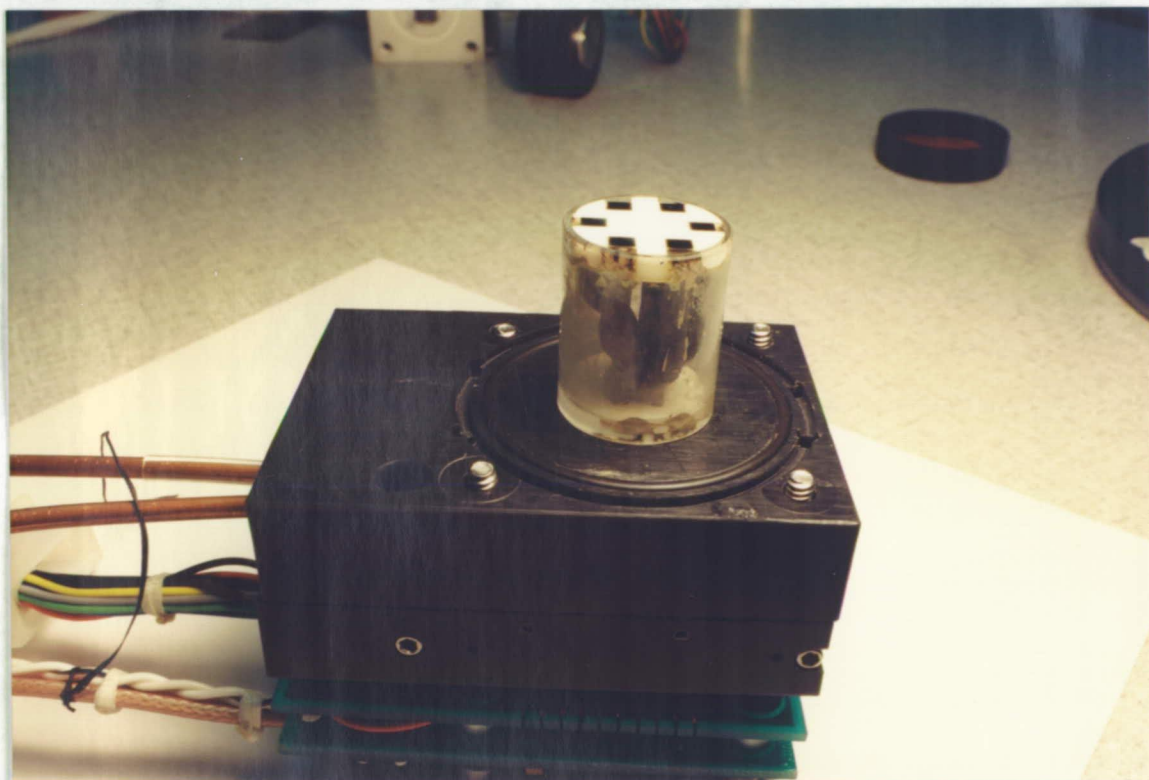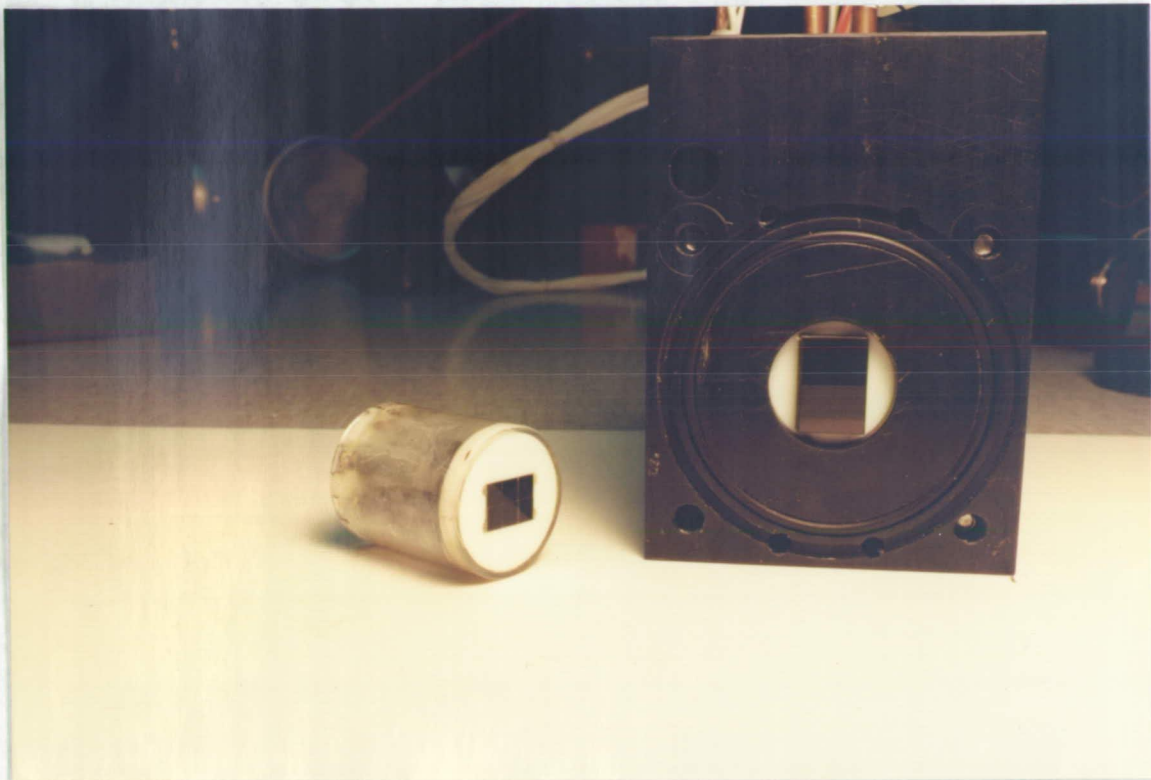
Figures 3 and 4. These photos show the CCD prepared in its housing. The image half is apparent in Figure 3. The coupler is sitting on the fiber window of the CCD in Figure 4. The coupler is made up in a glass tube of similar glass to the fiberoptic bundles. The ends of the bent fibers are gathered in machinable ceramic frames. This assembly was epoxied together, then polished.
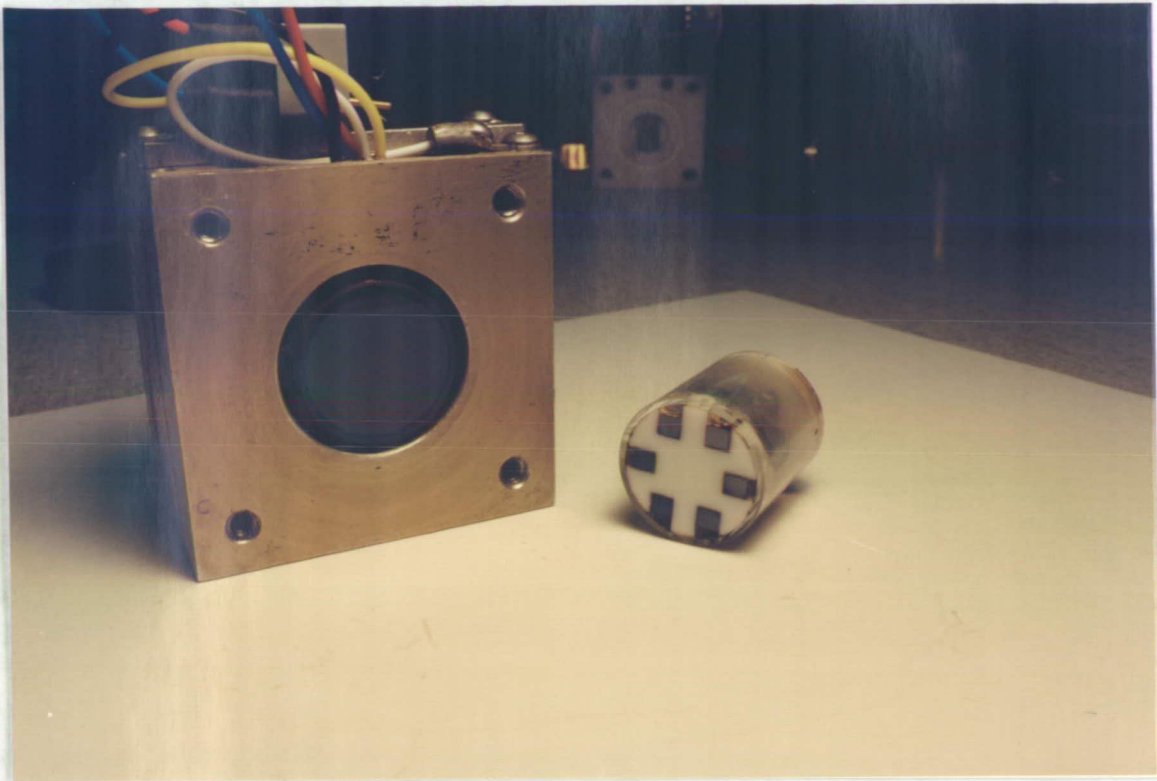
Figure 5. In this picture the back of the intensifier and the mating end of the fiberoptic coupler are shown.
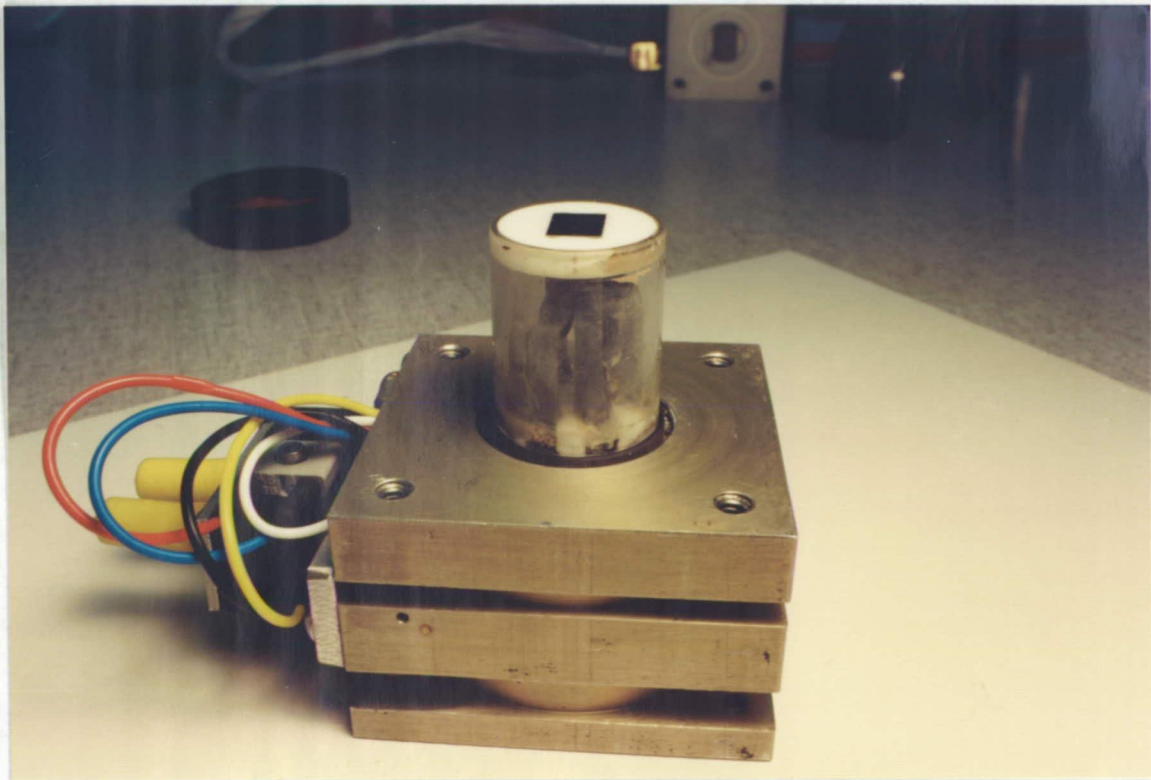
Figure 6. This picture shows the mating of the coupler to the intensifier window.
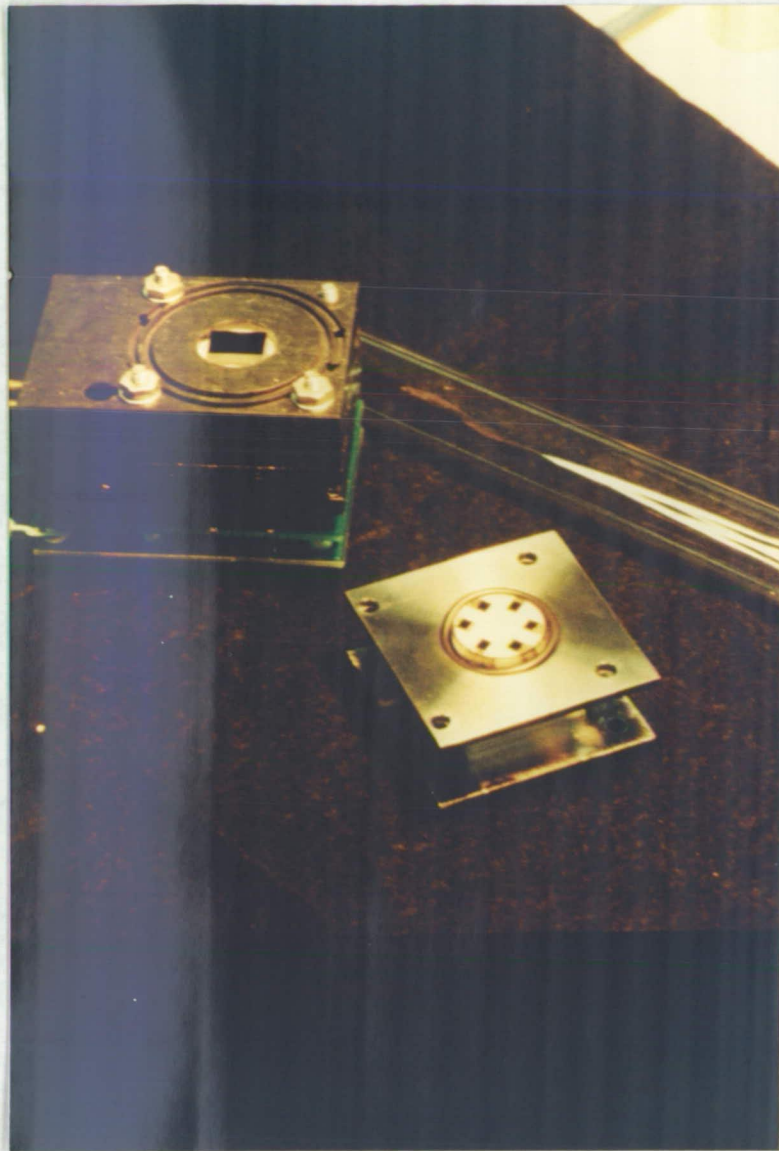
Figure 7. The fiberoptic coupler is mounted in a titanium fixture which allows the mechanical coupling to be completed. Titanium has the same coefficient of thermal expansion as the fiberglass.

APPLICATION OF THE ICCD TO AIRGLOW

AND AURORAL MEASUREMENTS

A. L. Broadfoot and B. R. Sandel

Lunar and Planetary Laboratory

University of Arizona

Tucson, Arizona 85721

April 5, 1991

ABSTRACT

New detector technology exemplified by advanced charge coupled device (CCD) and intensified charge coupled device (ICCD) systems have important advantages for both spectrographic and imaging research. However, to realize the full potential of this new technology, we must consider the detector and optical system as a whole. It is frequently not enough to simply substitute an ICCD for an earlier detector; rather, to achieve optimum results, the optics must be adapted to the specific detector. Properly designed spectrographs based on the ICCD detector offer the advantages of high throughput over a broad spectral range, precise wavelength stability, low noise, and compactness. Imagers having the wide field and high sensitivity needed for airglow research are practical as well.

I. INTRODUCTION

Quantitative auroral and airglow spectral measurements were first made by photographic emulsions in spectrographs and cameras. They recorded a great deal of information, both spectral and spatial, but had several important limitations. Photographic plates were slow, had limited spectral range, and were difficult to interpret quantitatively. Early electronic detection systems, such as the vidicon and image orthicon developed for the television industry [Rose, Weimer, and Law, 1946] did not provide a quantitative alternative. The development of the photomultiplier (Engstrom, 1947) was an important milestone.

The photomultiplier had sensitivity to single photoevents and the capability for high time resolution. Although the photomultiplier was about two orders of magnitude more sensitive than photographic emulsions, in a spectrograph it was limited to monochromatic samples. New optical designs were optimized for photomultipliers. By the early 1960's emphasis had shifted to monochromators (spectrometers) but the photographic spectrograph was still quite competitive when large spectral ranges and spatial resolution were required. Photometers with interference filters were useful as high-throughput monitors of a particular wavelength.

The most recent detector development has been in the family of solid state arrays, including charge coupled devices (CCD's), charge injection devices (CID's), Reticon photodiode arrays

(Timothy, 1983; Bredthauer *et al.*, 1988), etc. Although these devices have been available for nearly two decades, their application has been slow even though they have represented a major advancement in capability. We have been using the intensified CCD (ICCD) in our observational programs. They can be compared to the detectors mentioned above by noting that the intensified CCD's have the same sensitivity to photons as photomultipliers as well as the advantage of spatial resolution. With the ICCD instead of the photographic plate in a spectrograph, the spectrograph has single photoelectron counting capability, an improvement of about two orders of magnitude in sensitivity over the photographic plate. However, the full potential of this improvement cannot be realized by simply substituting the ICCD for the photographic plate; rather the optics must be re-designed, and adapted to the requirements of the new detector.

In this sense, the development of detector systems and scientifically useful applications are two different concepts. Several good review papers expound the details of the detectors under development (Timothy, 1983; Siegmund and Malina, 1983; Lampton, 1990). These descriptions do not come to grips with many of the practical aspects of application except in a futuristic way. Application in this paper will mean using available technology to make scientifically useful measurements. The distinction between application and development is important in the following discussions because the promises of detector development in the past ten years are very familiar while practical applications are very specialized. Few detectors qualify as candidates for use in general purpose instrumentation.

The astronomy community has taken a leading role in the application of CCD's to scientific measurement over the past one and one-half decades. The CCD's capabilities and shortcomings are well understood. In the use of intensified area detectors, astronomers again tried several techniques but improvements in the "bare" CCD progressed quickly enough to satisfy their requirements. The Voyager UV spectrograph launched in 1977 used an intensified linear array (Broadfoot and Sandel, 1977). It has undoubtedly the largest data base from which to study the application of array detectors that can record single photoevents.

The development work and application of CCD's over the past decade has resulted in understanding and confidence in the device. This is a result of both industrial and scientific interest in the CCD. Another device, the proximity focused image intensifier, using microchannel plates and a phosphor screen on a fiber optic output faceplate, has become readily available, and can replace the photomultiplier in many cases. This is also a proven product, resulting from military interest. Other detectors under development with various read out techniques do not fit into the category of proven and available. They fit into a class of special applications and in our opinion cannot be viewed as competing devices for general purpose use.

The intensified CCD is formed by fiber-optically coupling the output of the proximity focused image intensifier to the CCD to take advantage of the best attributes of both devices. The task is then a matter of engineering and verification rather than detector development. Here we discuss the use of intensified CCD's in two types of instrument that are suited for measurements of extended sources such as airglow and aurora, namely spectrographs and imagers, with major emphasis on the former. We compare their performance to alternative detectors, and discuss factors that must be considered in optimizing an observing program based on them. Among these are noise characteristics and suitable optical designs.

II. GENERAL CONSIDERATIONS IN THE APPLICATION OF CCD'S AND ICCD'S

The bare (unintensified) CCD has been used extensively in astronomy. The attributes of the device which have been most important are 1) linear response over several decades of dynamic range, and 2) the ability to integrate for long periods of time, hours at liquid nitrogen temperatures. The first is important because the data are in a digital format easily manipulated by computers. The second allowed the integrated signal from weak sources to exceed the threshold of sensitivity. The threshold was fairly high in the early days. The Voyager UVS detector (Broadfoot and Sandel, 1977) had a read noise of 10^4 electrons chosen as an easily attainable design criterion, although a level ten times better could be reached with special effort. Modern CCD systems exhibit read noise in the several electron range, approaching the ideal detector. However, they have other problems consistent with high sensitivity systems.

The intensified CCD has all of the attributes of photoelectron counting offered by the photomultiplier, including access to the whole photoelectric spectral range from 20-1200 nm but has been slow to be accepted as a viable detector system. We proposed the fiber optic coupling of a proximity focused imaged intensifier to a Reticon photodiode array for the Voyager spectrograph in 1971 following the work of Riegler and More (1973). The first ambitious application of the ICCD (Sandel and Broadfoot, 1976) was initiated in 1976 by these authors in the Imaging Spectrometric Observatory (ISO) proposed for Space Lab I (Torr, Basedow and Mount, 1983). Except for advancements in electronics, little has changed in our understanding of the ICCD as a detector system. It is not ideal, but it is readily available, has been used in several flight instruments, including the UV Imagers aboard the Viking Earth Satellite (Anger *et al.*, 1987; King *et al.*, 1988) and is very flexible in configuration.

The CCD and the ICCD differ considerably in use. A primary consideration in selecting between them is their threshold of detection for a given integration time. For simplicity, we will assume in the following discussion that the CCD and ICCD have identical quantum efficiencies thereby generating photoelectron events at equal rates. The CCD is basically an analog detector but its sensitivity is high enough that it is evaluated by single photon (electron) statistics. The read noise is typically 10 to 50 e^- (electron hole pairs) rms and in special cases it has been reported to be < 10 e^- rms. The signal-to-noise ratio ρ for a read of a single pixel may be written as

$$\rho = \frac{S}{\sqrt{N+D+S}} \tag{1}$$

where S is the number of electron-hole pairs generated by the signal, D is the number resulting from thermal dark count, and N represents the contribution from the read noise of the electronics. We take N to be the square of the rms read noise. Figure 1 shows curves of ρ for a range of values of S.

The intrinsic dark count rate of the photon-counting ICCD is very small on a per-pixel basis. For example, the dark count rate of a cooled S-20 photocathode of diameter 25 mm is typically 10
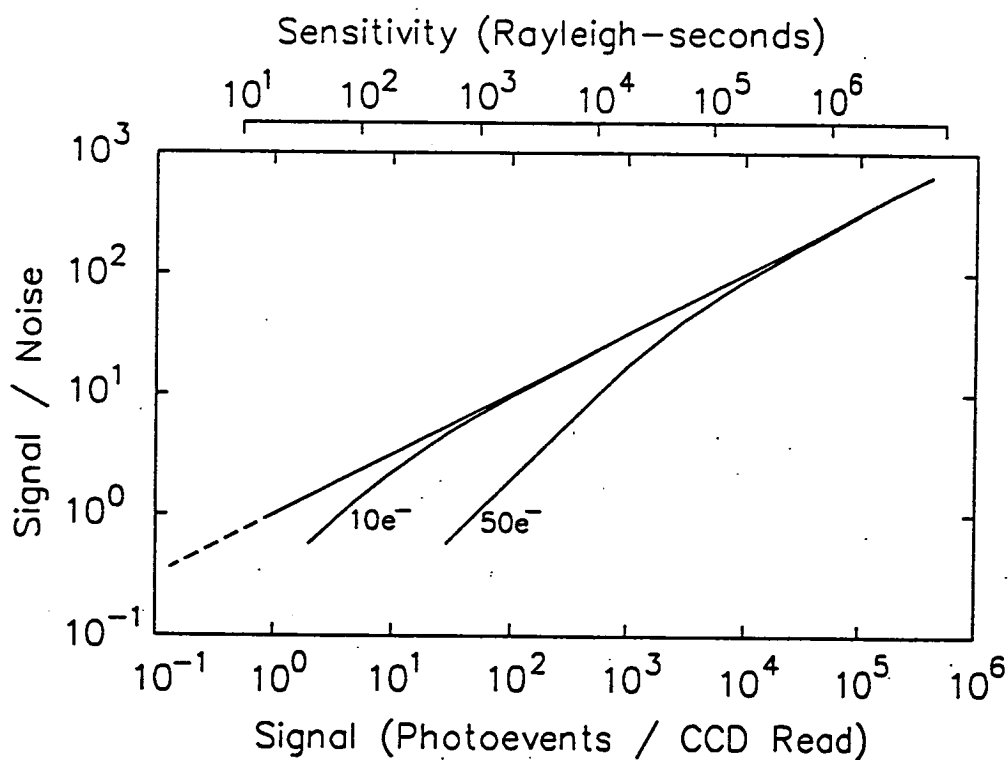
Figure 1. Signal-to-noise ratio p for CCD and ICCD detectors computed using equation 1. The straight line represents the ICCD, for which N is effectively zero because of the photo-electron counting capability of the ICCD. The curved lines represent CCD systems having readout noise of 10 and 50 electrons.

events/second. Scaled to the $5x10^{-4}$ mm^2 area of the pixel this corresponds to $\sim 10^{-5}$ events pixel^{-1} sec^{-1}. Cathodes with reduced red response (higher "work function") are less noisy. The ICCD curve, in the interesting range of the CCD curve, is a straight line. In Figure 1 the ICCD curve was drawn through S/N of 10 and 100 then extrapolated through 1 without regard for the statistical implications since individual photoevents can be detected by the ICCD.

It is interesting to consider the meaning of the threshold of detection for each detector system. The photoevent-counting intensifiers are the most straightforward. The noise is dominated by the shot noise in the signal. Long integrations give the same results as the summation of multiple short samples representing the same total integration time. On the other hand, the read noise and other effects in the operation of the CCD do limit the threshold sensitivity. With the CCD the most effective way to increase ρ is by increasing the integration time; astronomers use hours. If adjustment of the integration time is not acceptable, two other approaches can improve the statistical performance modestly. They are referred to as "on-chip summation" and "off-chip summation."

For photon counting detectors, both techniques (on-chip and off-chip summation) result in improved statistics. The photoevents appear as a burst of up to 10^3 e$^-$ in the CCD. This charge overwhelms the lower level of noise associated with normal CCD readout. Event counting statistics will prevail. (Figure 1.) This is not the case for the bare CCD.

On-chip summation sacrifices spatial resolution to minimize the number of read operations required to measure the charge on the chip. The technique is to move the charge in several adjacent pixels into the output junction, then sample and digitize the accumulated charge with a single read. Although this improves the signal-to-noise ratio over the sensitive area, the question of interest here is the effect on the threshold of detection. For example, if ten pixels each having a signal charge of 50 e$^-$ are summed on-chip the resulting signal to noise ratio should be 10. If each pixel had an average of only 5 e$^-$ and were shifted into the output junction, would the result be a signal to noise of unity? There is the question of efficiency in handling a 5 electron charge. We do not know of work which deals specifically with the effect of moving very small numbers of charges. In any case, there are other noise contributions which become significant at this level of on-chip

summation (see Janesick et al., 1985). Any leakage charge on the pixels would be summed into the output gate as well the signal charge. It appears that there would be difficulties in pushing the threshold down very far with the on-chip summation technique.

Off-chip summation also has limitations when the signal is close to threshold. First, the S/N improvement follows the square root law in this case. Although areas which have identifiable intensity structure will improve in S/N, it is unlikely that the summation of samples with a S/N of unity or less will result in a recognizable improvement in threshold of detection. The effect of reducing the read noise to 10 e$^-$ is shown in Figure 1 but the considerations above are still valid in evaluating the threshold of detection at the 10 e$^-$ level.

We argue that the two devices, the CCD and ICCD, can be separated in their application by their threshold of detection. For continued discussion we will assume that the CCD has a threshold of detection of about 50 photoevents for comparative purposes. Also, we will assume that each pixel of an ICCD can be considered as a photon-counting device that preserves the Poisson statistics of the arriving photons.

The dynamic range of the detector is generally not a limitation for either CCD approach. The limitation in dynamic range in many cases is caused by internal scattering in the optical system and not the detector. The bare CCD has a linear response from its threshold to pixel saturation. Depending on the threshold and the "full well" charge capacity of the pixel, the dynamic range can be greater than 10^4. Saturation of some pixels does not affect the rest of the pixels significantly. This dynamic range is sufficient for most applications and it can be extended by exposure control.

The ICCD dynamic range is not restricted by the detector either. It is defined by a companion digital memory and the dark count rate rather than by the full well capacity. At maximum gain, the intensifier generates about 500 e$^-$ per photoevent in a CCD pixel. This implies a dynamic range of 500 events for a full well capacity of 2.5 x 10^5 e$^-$, but the CCD can be read out often and the events accumulated in a companion memory. High signal levels can also be handled by reducing the gain of the intensifier. The good statistical accuracy implied by the high photoevent rate is maintained by integrating the signal on the CCD; the only statistical penalty is a factor of

$2^{\frac{1}{2}}$ introduced in the transition from pulse counting to pulse integration. The Voyager UV detector can integrate signal on the anode array when the MCP is operated at low gain. The result is a markedly extended dynamic range. When the Voyager UVS observes the sun, it measures photoevent rates up to 3×10^4 photoevents sec^{-1} $pixel^{-1}$. At full gain, photoevent rates of 5×10^{-3} sec^{-1} $pixel^{-1}$ are routinely recorded at our threshold of detection. The full dynamic range is therefore about 10^7. The threshold of detection for the Voyager UV Spectrograph detector is similar to that of the ICCD detector system, 10^{-3} events/second. This threshold is higher for the photocathodes that generate appreciable dark noise.

The ability to deal with high signal rates is not usually the concern in typical scientific applications. Rather, the limiting factor is usually the ability to deal with weak signals. Scientific observations are most often driven to the statistical limit to improve temporal, spatial, or spectral resolution.

III. THE APPLICATION OF AREA DETECTORS TO THE SPECTROGRAPH

In the following discussions we concentrate on the use of the ICCD for aeronomical measurements, comparing it to other detectors which have been used for that purpose. We consider also the "bare" CCD, but the need for short integration times in most aeronomical observations leaves the bare CCD a poor contender.

There are five important differences between the ICCD spectrograph and the photomultiplier monochromator which we touch on in the following sections: (1) Optical design criteria are different. (2) The optical throughput or "speed" of the spectrograph for obtaining a complete spectrum is improved by about two orders of magnitude due to the multiplexing nature of the detector. (3) The size of the instrument can be decreased by a factor of 10 in focal length or 10^3 in volume in many applications. (4) The effective dark count rate per pixel is reduced by at least two orders of magnitude. (5) Quality of the data is improved remarkably, because the spectrograph need have no moving parts. The specific application will determine the degree to which these improvements can be achieved but in general the advantages are almost revolutionary.

A. Optical Designs and the ICCD Detector System

In a previous section we noted that the development of the photomultiplier resulted in a change in the optical design of spectrographic instruments to take advantage of the photomultiplier. The area detector also requires special optical designs. There will be a return to the spectrographic configuration but with some new constraints.

Spatial and spectral information can be obtained from the spectrograph, but this requires a good quality image of the entrance slit in the image plane of the "camera" system. (Typically there are three imaging optical elements defining a spectrograph: the collimator, the dispersing element, and the camera.) The optics for a monochromator need only image the width of the entrance slit on the exit slit for good performance; a one-dimensional or astigmatic image will suffice. Fastie (1952) was quick to rediscover the "Ebert monochromator" which had not seen much use since its original description (Ebert, 1889), presumably because the severe astigmation in the system was unsatisfactory for a spectrograph. Fastie pointed out that the Ebert-Fastie optical system could cancel spherical aberration and greatly reduce coma by the use of complementary spherical surfaces for the collimator and camera optics, and a special curved slit geometry. The reflecting optics have no chromatic aberration. The result was a high throughput high resolution monochromator, the Ebert-Fastie. However, the curved slit and astigmatic optics are inappropriate for the rectangular format of the CCD. Although the Ebert-Fastie optical system is "fast," recording the full spectrum in a single exposure on the ICCD has an advantage of about two orders of magnitude over the Ebert-Fastie monochromator. This is best illustrated by a direct comparison of the Ebert-Fastie monochromator and a comparable ICCD spectrograph.

The performance of a monochromator or spectrograph viewing an extended source can be estimated using the photometric equation:

$$P = B_\lambda \, A_d \, \frac{A_g \cos \phi}{F^2} \, \tau \, \eta \, \epsilon \tag{2}$$

where

P is the photoevent rate in events sec^{-1} $pixel^{-1}$,

B_λ is the brightness of the source in photons sec^{-1} cm^{-2} $ster^{-1}$,

A_d is the area of the detector,

(A_g cos ϕ) is the effective area of the grating of area A_g

operating at an angle ϕ,

F is the focal length of the camera lens,

τ is the optical transmission,

η is the efficiency of the dispersing element, and

ϵ is the quantum efficiency of the detector.

The following discussions can be simplified by some substitutions to equation (2). The area of the detector can be replaced by the effective dimension of the exit slit, L, the length of the slit and, W, the width. The grating area divided by the focal length squared is a solid angle and can be replaced by the reciprocal f-ratio of the camera optics squared,

$$\frac{A_g \cos \phi}{F^2} = \frac{\pi}{4} \frac{1}{f^2}$$

The modified photometric equation is

$$P = B_\lambda \frac{\pi}{4} \frac{LW}{f^2} \tau \eta \epsilon \qquad (3)$$

For this comparative study we assume that the transmission of the optical system τ, the grating or dispersive efficiency, η, and the quantum efficiency, ϵ, are equal in the two systems. When the constant terms are collected into the constant k, the expression becomes

$$P = k \frac{LW}{f^2}, \qquad (4)$$

and from system to system the throughput, E, has the proportionality

$$E \propto \frac{LW}{f^2} \qquad (5)$$

This can be made specific by comparing the performance of an Ebert-Fastie 1/8-meter monochromator with that of a spectrograph having equivalent resolution, spectral range, and f-ratio,

but designed around the ICCD. The two optical systems are shown in Figure 2. Table 1 lists the characteristics of the two designs.

Table 1. Monochromator/Spectrograph Comparison

	E-F monochromator	Area Detector (ICCD) Spectrograph
Focal Length (F)	125 mm	125 mm
f-ratio (f)	5	5
Resolution	10Å	10Å
Grating	3600 1/mm	530 1/mm
Slit Width (W)	0.45 mm	0.066 mm*
Slit Length (L)	12 mm	8.5 mm
Spectral Element	3.3 Å/step	3.3 Å/pixel
Range	1900 Å	1900 Å
Elements/spectrum	576	576
Optical Throughput (E) (Monochromatic)	9.6	1
Optical Throughput for full spectrum	1	60

*The spectrograph has no physical exit slit, but the function of an exit slit is performed by the discrete pixels of the ICCD.

The two sets of design parameters have been selected to produce identical spectra. The focal length and f-ratio were taken from the E-F design. A high-dispersion grating maximizes the throughput of the monochromator and three grating steps/slit width were used. To match this the ICCD system has 3 pixels per slit width and a grating ruling selected for a dispersion of 3.3 Å/pixel. The spectral range was determined by the number of rows in the ICCD array so that each spectrum would contain 576 samples.

Since the f-ratios are equal in the two instruments, their monochromatic throughput is simply the ratio of the areas of their slits. The E-F slit is 9.6 times larger than the slit in the ICCD spectrograph. However, in order to cover a range of 1900 Å at the specified resolution, we must step the E-F grating and integrate 576 times. Hence we must consider the rate at which information is recorded, and find that the spectrograph will produce 60 spectra while the E-F monochromator produces a single spectrum of comparable quality. Not only does the spectrograph gather photons 60 times faster than the monochromator, but the quality of the data is improved.

PM Tube ⌐   ⌐ Entrance Slit ⌐

2-D
Detector

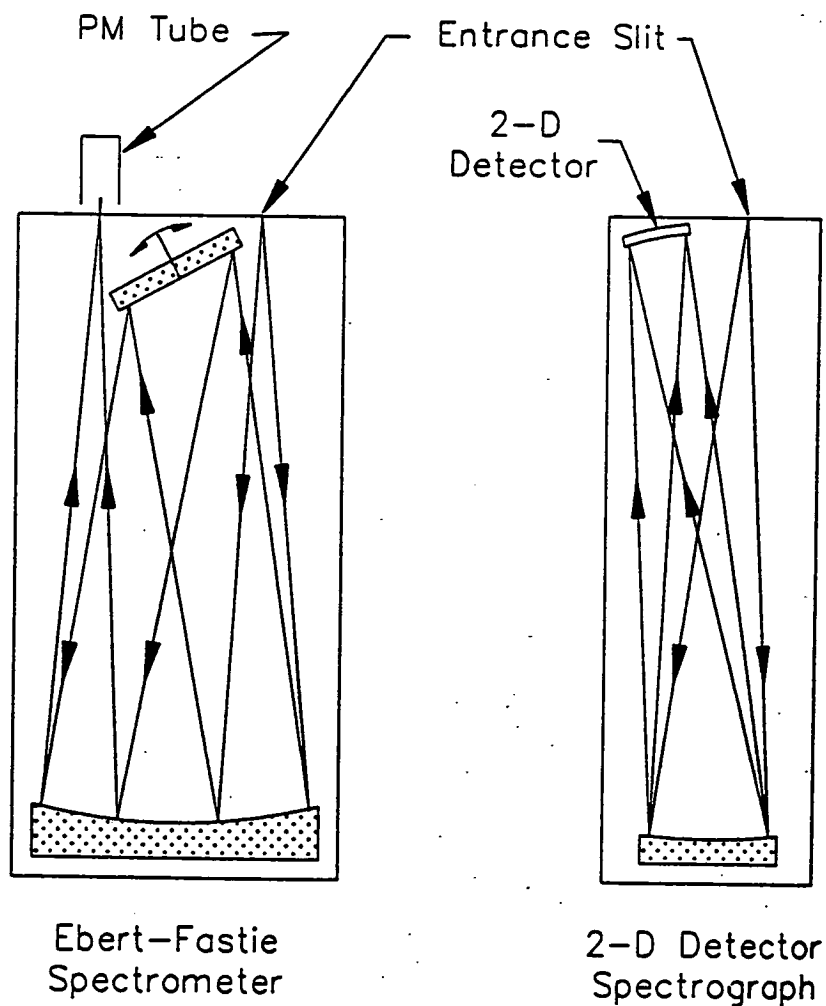Ebert—Fastie
Spectrometer

2-D Detector
Spectrograph

Figure 2. Comparison of a conventional Ebert-Fastie spectrometer with a spectrograph designed to take advantage of modern 2-dimensional detectors. In terms of the time required to cover the same range of wavelengths at equivalent resolution and statistical accuracy, the spectrograph has an advantage of a factor of 60.

Scattered light in the spectrograph is lower by the ratio of the areas of the slits, a factor of 9.6. The detector and optical system of the spectrograph have no moving parts, so internal scattering depends only on the input of illumination and can be measured for later removal. Temporal variations in the source are recorded over the entire spectrum simultaneously. The spectrograph images the entrance slit on the detector, so spatial variations in the source will be recorded. All of the advantages of spectrographs with photographic plates can be realized in the ICCD spectrograph.

Flexibility and small size are additional advantages to the ICCD spectrograph. The optical design of the E-F system is fixed and the experimenter can use only the fore-optics to adapt the instrument to the observation. This is not the case with the ICCD spectrograph. The entire optical train is at the designer's disposal. It is most important to realize that the optical design of an ICCD system is constrained by the size of the detector and therefore high speed does not necessarily imply a large instrument. The quantities L and W are the dimensions of the pixel array on which the entrance slit will be imaged and are therefore constrained by the detector size. The f-ratio refers to the camera feeding the detector. The throughput will be constant as long as the f-ratio remains the same *regardless of the size of the optics*. In practice the size of the optics can be reduced until the image quality over the area of the detector becomes unacceptable due to the optical aberrations in the system. It is also noteworthy that the throughput is not affected by the speed of the optical system in front of the grating provided it does not vignette the camera system. The f-ratio of the collimator can be very large compared to that of the camera. A large f-ratio has the advantage of better scattered light control in the spectrograph. The f-ratio can be reduced until the image quality at the edge of the array becomes unacceptable.

The example above can be extended to instruments used in the past. A variety of instruments that have seen substantial use over the past two decades are cited to illustrate the utility of area detectors. Beginning with the basic instrument design, we have adjusted the parameters of each instrument to give the same spectral resolution in the 400 nm region of the spectrum. Then we have evaluated the constant in equation (4) for each instrument to place the comparison on a common photometric scale. The characteristics of the instruments have been gathered in Table 2.

The slit widths of the monochromators were chosen for 3 Å spectral resolution assuming the use of a 1200 line/mm grating in second or third order as indicated. The spectrographs have their resolutions set by the pixel size and slit width; the slit width in the image plane was taken to be 3 pixels. In this case the ruling of the grating would be adjusted to give the correct linear dispersion; note that only this apparent slit width enters the calculation of sensitivity. Spectrograph E, an objective grating spectrograph similar to the Voyager UV instrument, can be included in the comparison because the calculation is independent of wavelength. At EUV wavelengths reflective efficiencies are very poor requiring a trade-off between resolution and throughput. Spectrograph F refers to an ICCD spectrograph which has been recently put into service by the authors. Called the Arizona Imager/Spectrograph (AIS), it was built for the Air Force Geophysics Laboratory and will be flown on the Shuttle. Details of the instrument are given in a companion paper. A compromise in throughput by a factor of 4 was accepted to allow the spectral range 115 - 900 nm to be recorded simultaneously with 4600 spectral elements. The slit width is 2 pixels. Spectrograph G is the same as spectrograph F, but designed to have full throughput with a slit width of 3 pixels as in the comparison with the Ebert-Fastie spectrometer above.

Spectrograph H is a more special case. It is the same as spectrograph F except that it has a bare CCD rather than ICCD in the image plane. The read noise of the CCD is a limiting factor as noted above. Even though there are nearly 1800 pixels within the effective slit, there is a read noise of 50 e$^-$ associated with the reading of each pixel. The sum of all samples would give an effective read noise of 50 x $\sqrt{1800}$ = 2000 e$^-$ requiring a signal of 2000 e$^-$ to provide $\frac{S}{N}$ = 1. On-chip summation of 18 pixels per read followed by off-chip summation would result in an effective noise threshold of 500 e$^-$, the number used in Table 2.

The comparative study is completed by estimates for a photographic spectrograph, I. Vallance-Jones, 1974, comments on high speed photographic spectrographs. For an instrument developed by A. B. Meinel in the early 50's and used with an f/0.8 Schmidt camera, he suggested a sensitivity in the 10^5 R-s range as a reasonable working value, and estimated the threshold of sensitivity to be 10^4 R-s.

The sensitivities in Rayleigh-seconds from Table 2 are plotted in Figure 3. The Rayleigh-second (Vallance-Jones, 1974) is the emission rate required to produce a signal-to-noise ratio of unity in one second. The calculations whose results are shown in Table 2 treat each instrument as a monochromator having one spectral element. As the spectral range for monochromators A, B, and C increases, the sensitivity decreases proportionally because time must be shared among the other elements of the spectrum. On the other hand, the spectrographic instruments have roughly the same sensitivity at each spectral resolution element.

There are many techniques for optimizing an instrument for a specific observation. Since the requirement in future programs is for broad spectral coverage, it seems that the ICCD system will be most useful. The airglow atlas of Broadfoot and Kendall (1968) was accumulated in segments of 500 spectral elements with monochromator B. Figure 3 shows that an equivalent spectrum of 576 spectral elements would be recorded by an optimized ICCD spectrograph (G) about 200 times faster than with monochromator B. The AIS spectrograph (F) will record the same spectrum of 500 elements 32 times faster but in addition will record a much wider spectral range, including 4600 spectral elements at once. This is a spectacular improvement in capability. The rating of the CCD spectrograph (H) with respect to the optimized ICCD spectrograph (G) is noteworthy. The ICCD spectrograph (G) seems to be 316 times faster than H on the basis of this comparison. It can be argued that we have not treated the CCD spectrograph fairly but even factors of two or four do not bring the CCD spectrograph into contention. It has been demonstrated that the improvements discussed above are attainable in practice, but that demonstration will not be discussed in detail here.

B. The Size of ICCD Spectrographs

In the discussion of optical designs and the ICCD spectrograph it was mentioned that the design is constrained by the size of the ICCD format. This conclusion follows directly from the equation 5. The proper length and width for the slit image are determined by the CCD format and are therefore constant, leaving only the dimensionless f-ratio as an adjustable parameter. The comparative study in the previous section addressed the performance of several instruments whose focal lengths ranged
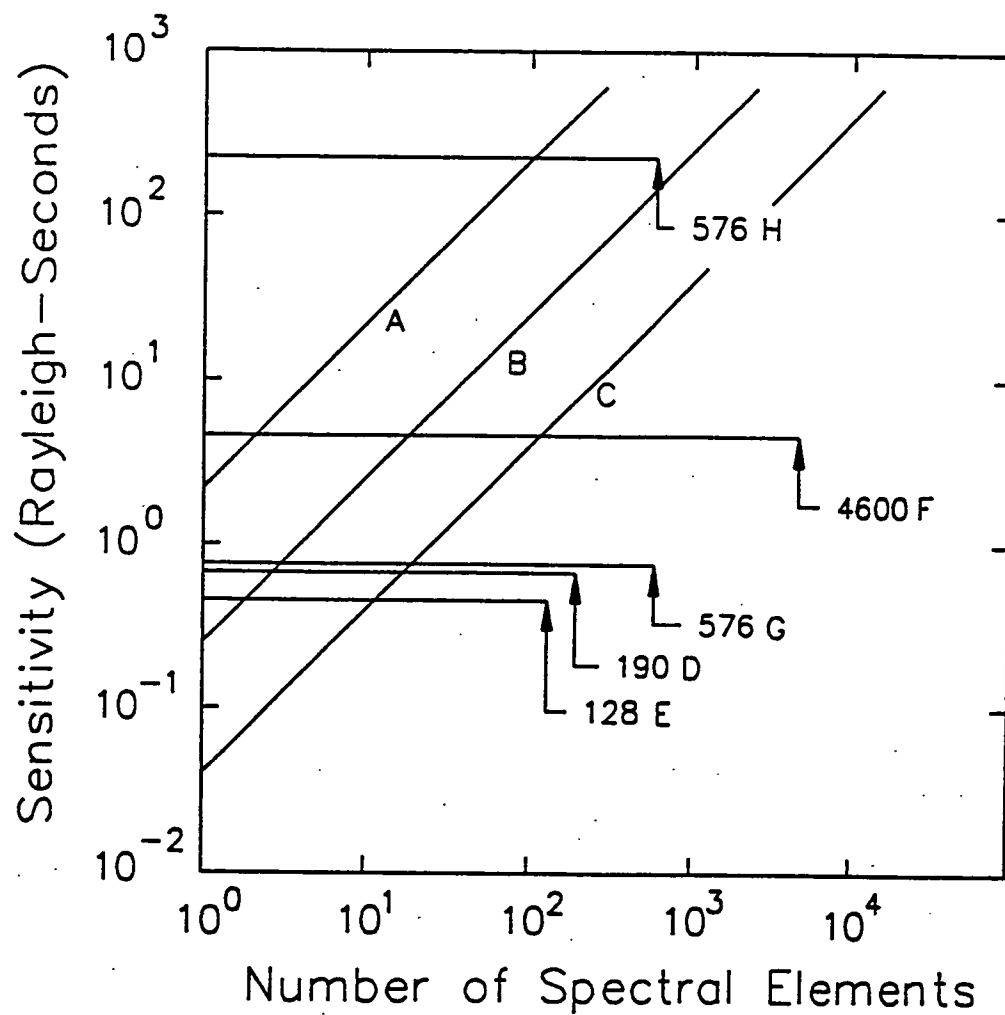
Figure 3. Sensitivities for the instruments listed in Table 2. The letters labeling the lines match those in the table. The numbers show the number of spectral elements in each spectrum. The sensitivities of the monochromators depend on the number of spectral elements because of the necessity for time-sharing.

over an order of magnitude, from 100 cm to 10 cm. The monochromator performance scales by focal length while the performance of the spectrographs scales by array size. Note also that performance was improved by orders of magnitude in the short focal length instruments that can record broad wavelength regions.

A difference of a factor of ten in focal length implies a difference of a factor of 1000 in instrument volume. For example, a standard commercial 35 mm camera lens such as the Nikon 135 mm f/2, with a 50 mm square grating and a modest collimator and slit, forms a very small spectrograph. The smaller f-ratio would improve its performance by a factor of 2 over the ICCD spectrograph G in Table 2. Although it would be limited in spectral range by the lens coating, the comparison in size and performance are remarkable.

The application of new technology has completely reversed the emphasis in instrumentation. The monochromator was a precision, high-cost optical tool with a read out system as simple as a photomultiplier tube and strip chart. The array detector allows the use of simple optical configurations but the data retrieval and manipulation require major resources. However, once the data analysis system has been established, the spectral coverage required in future programs can be achieved by a replication of small spectrographs covering the spectral range and having a common data format. At the University of Arizona this technique is used to provide small flight spectrographs in a group of 5 to cover the wavelength range from 115 nm to 1100 nm simultaneously with 4600 spectral elements. The spectral resolution varies from 3 to 10 Å over the spectral range. The spectrograph set has outside dimensions of 41 x 41 x 21 cm. This instrument is described in a following companion paper. The spectrographs are included in Table 2 and Figure 3 as Spectrograph F.

C. Data Quality Comparisons

Not only does the ICCD spectrograph have a photometric advantage over monochromators, the quality of the data shows a remarkable improvement as well. The data set accumulated by the Voyager UV spectrograph can illustrate this point. Since the detector integrates signal continuously over the whole spectral range, it records temporal variations in the relative brightness of features

within the passband properly. Also, the effects of internal scattering and other characteristic contaminations are recorded simultaneously with the primary emissions.

The monochromator lacks this advantage because only one wavelength position is sampled at one time. The recorded signal includes not only the selected wavelength but also a scattered contribution from other bright regions of the spectrum. The scattered component cannot be determined with confidence, because the emission causing it is not recorded simultaneously.

The Voyager UV Spectrograph presents a unique opportunity to evaluate a photoevent-counting spectrograph. It has no moving parts. It records the spectrum from 500 to 1700 Å in 128 segments with an intensified Reticon linear anode array. Although this spectral range may be unfamiliar to many workers, the data are characteristic of the photoevent-counting spectrographic capability at any wavelength.

Figure 4 shows a Voyager UVS spectrum of emissions from the interstellar medium acquired in the direction of the galactic pole, a region free of stars. The integration time was 1.5×10^6 seconds or about 415 hours. The emissions arise from resonance scattering of solar lines by interplanetary hydrogen and helium (Holberg, 1986). The He(584 Å), H(1216 Å) and H(1025 Å) lines are well defined. Note that the ordinate scale changes through the analysis. The H(1216 Å) line intensity results in a peak photoevent rate of about 1 sec^{-1} pixel^{-1}. Laboratory calibration of the instrument measured the scattering from lines at many wavelengths throughout the wavelength range. After the detector dark count is subtracted, a matrix multiplication removes the effects of scattering of the four emission lines He(584 Å), HLyα, HLyβ, and HLyγ. The resulting spectrum is shown in Figure 4b. In Figure 4c this reduced spectrum is compared with a model computed by a spectral synthesis program which applies the instrument's transmission function to the four discrete lines. Using these techniques we have found that the modeling process gives a sensitive measure of wavelength. Although each spectral element is about 9 Å wide, the model line must be placed within 2 Å of the true wavelength position for a match to be convincing. Figure 4d shows the difference between the model and the reduced spectrum in 4c. This represents the noise in the observation after the emission is removed. Differences are large where the signals are larger even
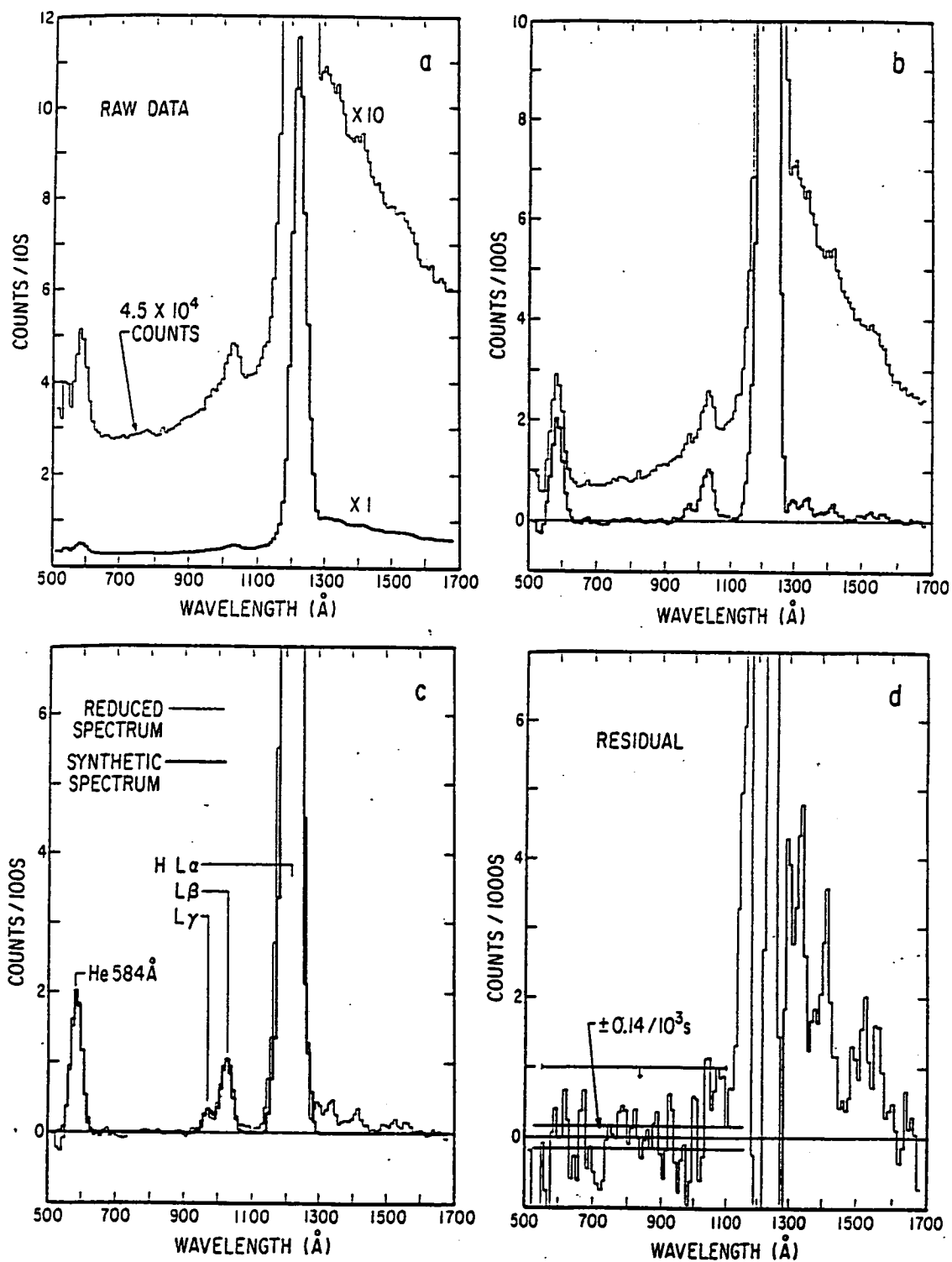
Figure 4. An illustration of the steps leading to a final spectrum from a spectrograph (after Holberg, 1986). Panel a: Raw spectra including signal and detector background. The detector background is due to intrinsic noise and to gamma rays from the radioisotope thermoelectric generators that power the spacecraft. Panel b: Result of subtracting detector background (top curve) and removing instrumental scattering (bottom curve). Panel c: Comparison of lower curve in panel b with a synthetic spectrum composed of He 584 Å and H Lyman series lines. Panel d: Residual after subtracting data and synthetic spectra in panel c.

though the percentage error is decreasing. In Figure 4a the count at about 750 Å is about 4.5×10^4 counts channel^{-1} in 1.5×10^6 seconds. Poisson statistics imply a corresponding standard deviation of 212 events or ±0.14 events in 1000 sec. That envelope, illustrated in 4d, is very close to the envelope of the noise left after the analysis. This demonstrates that it is possible to understand the origin of all events in the spectrum, to the statistical limit of the observation. Finally, the event rate for the peak in the H Lα line was 1 per second while the rate for the H Lγ line peak was 1 in 330 seconds; the usable dynamic range for these spectra was therefore at least 330. Similar work can be done with photoevent counting systems having higher sensitivities and higher counting rates limited only by the statistical accuracy of the weakest emission as noted above.

IV. THE APPLICATION OF AREA DETECTORS TO IMAGING

The astronomy community took the lead in the application of the CCD to research imaging. Again this was an expensive undertaking requiring the development of new electronics techniques, the evaluation of sensors, and the development of image processing systems. However, their application had rather modest requirements for success; the CCD was in direct competition with the photographic plate. Even the early CCD devices and systems enjoyed important advantages in detector capability. Although this technology was an important advancement holding great promise in astronomy, long integration time and broad spectral band were acceptable. In contrast, the airglow and auroral community requires higher time resolution and narrow band photometry, and the bare CCD has proven less useful. The interference filter and photomultiplier had replaced photography as a scientific tool in the early 60's. Monochromatic imaging was pursued using flying spot photometers. Intensified photography has seen modest use in the past few years, followed by some use of intensified solid state detectors.

The requirements of the astronomical application and airglow and auroral application differ. For the purpose of this discussion it is appropriate to compare on the basis of angular resolution. When an f/3 telescope with an aperture of 4 meters and a focal length of 12 meters illuminates a single CCD pixel 0.022 mm square, the pixel has an angular field of view of 0.4 arc-sec. If the field of view is filled by a radiating nebular gas as well as the airglow in the foreground, the signals

will be proportional to the surface brightnesses. The surface brightness of the nebular gas may change from pixel to pixel with changes in gas density or excitation. The airglow brightness would contribute to each pixel uniformly since the field of view is small compared to the scale of variations in airglow emissions. When the optical system is scaled down by a factor of 10^3, to an aperture of 4 mm and a focal length of 12 mm, the same pixel has an angular field of 0.1°. The nebular source would be contained in a small fraction of the field of view with the detected radiation reduced proportionally. However, the airglow still fills the field of view of the pixel and the signal level will be the same as for the larger system since the photometric expression (5) is the same for both optical systems. The brightness of the airglow might vary from pixel to pixel depending on the source of the emission.

We make these comparisons for two reasons. The first is to emphasize that the significant feature of an image is the variation of intensity over the field. It is important to select the angular field to match the scale of the intensity variation to be measured. The second is to emphasize that the photometry is independent of the size of the optical system.

The discussion of the threshold of detection of the ICCD and CCD can be placed on an absolute scale for this imaging review. If an optical system has the following parameters:

f-ratio	1
Pixel area	$(2.2 \times 10^{-3} \text{ cm})^2$
Transmission, τ	0.9
Quantum Efficiency, ϵ	0.2

then for unit emission rate, $1 \text{ R} = 10^6/4\pi$ photons $\text{sec}^{-1} \text{ cm}^{-2} \text{ sr}^{-1}$, in equation (2) the photoevent rate is 5.4×10^{-2} events $\text{pixel}^{-1} \text{ sec}^{-1}$. The abscissa of Figure 1 can be converted to the sensitivity scale at the top of the figure using this factor. For instance, an emission rate of 18.5 kR would generate 10^3 photoevents $\text{pixel}^{-1} \text{ sec}^{-1}$. The threshold arguments made previously can now be considered on an absolute scale. The sensitivity of the CCD imager would be about 1 kR-s. A surface brightness of 1 kR would produce 50 e^- pixel^{-1} in a one-second exposure, the previously defined threshold of detection. For the ICCD the corresponding number would be 18 R-s.

A. Broad Spectral Band Imagers

Many of the dominant auroral emissions can be monitored with interference filters of reasonably wide bandpass (e.g. 50 Å) which could be incorporated into the fast f/1 optical system used as a baseline in the discussion above. Even with the 1 kR-s threshold of the bare CCD, typical auroral emissions, which are usually tens of kR, would give detectable signals in a one-second exposure. The 0.1° angular resolution of a single pixel corresponds to a scale of 200-400 meters at typical auroral heights and ranges. An array of 100 by 100 pixels corresponds to a field of view 10° square, a size useful for comparative studies of auroral morphology. This type of imager would also be useful for support imaging during spectrographic observations. Clusters of 4 or 6 miniature imagers are quite feasible using fiber optic technology and CCD arrays. For weaker aurora where requirements for both time and spatial resolution can be relaxed, both longer exposures and on-chip summation of 4 or 9 pixels would produce images of good signal-to-noise ratio. Intensified systems would be required for better time resolution, but these can also be implemented in a clustered set.

The imagers associated with the spectrographs in the companion paper (Broadfoot et al., 1991) were prepared following the outline above. Twelve miniature images are recorded by two CCD's using fiber optic coupling; ten of these are intensified.

B. Monochromatic Imagers

For narrow band monochromatic imaging, the need for near-normal incidence on the interference filter constrains the f-ratio of the optical system. In this case maximized throughput is important because these imagers are often used to separate weak emissions from a complicated spectral region. The optical technique is to use the largest interference filter available. An image of the sky is formed on the filter through telecentric optics. This image is then re-imaged on the intensifier. To maintain the pass band of an interference filter with a 5 Å bandwidth, the incidence angle θ must not exceed about 4° from the normal. The required f-ratio of the fore optics is given by $f = (2 \tan \theta)^{-1}$ which implies an f/7 system for the example given here. If the optics are properly designed, the f-ratio of the fore-optics can be converted to an f/1 system feeding the

CCD. This will result in a system with the sensitivity defined by the ICCD curve in Figure 1 if the f-ratio transition is made without vignetting. (Some corrections are required for optical transmission and quantum efficiency.) A sensitivity near 40 R-s would be typical. Again by sacrifice of spatial resolution through on- or off-chip summation of 2 x 2 or 3 x 3 pixels, the signal could be increased by factors of 4 and 9 respectively; this is effectively increasing the area of the pixel.

Still higher sensitivities can be achieved by a further increase in the effective area of the detector. This can be achieved with the ICCD by use of larger proximity focused intensifiers, say 40 mm diameter, with the output image reduced by a fiber optic taper to 15 mm diameter to fit the CCD array.

C. Application to the Fabry-Perot Interferometer

The Fabry-Perot interferometer falls in the same category as the monochromatic imager, but its field of view is still narrower and large plates are used to increase the collection area. The optical coupling problem is the same as for the monochromatic imager; a high-speed telescope would be used with an aperture the size of the F-P plates. The focal length of the telescope would determine the number of rings falling on the CCD. Each spectral order in the F-P fringe pattern contains the same energy. The improvement over the classical scanning F-P system can be evaluated by counting the number of rings and the number of elements required across the ring. An operational advantage lies in the ability to find the center of the ring pattern with software rather than by adjusting the plates and ring position.

In an earlier section we commented on imaging the aurora through passband filters with a CCD. In this section we discuss the threshold of detection and the ICCD in connection with data from a specialized application. The image of Comet Halley in Figure 5 was obtained with a telescope and Fabry-Perot interferometer matched to an ICCD by appropriate optics (Magee-Sauer *et al.*, 1988). The interferometer isolated the cometary OI (6300 Å) emission, which was Doppler shifted from the Earth's airglow line. The intensity gradient from the background to the nucleus of the comet is clear. Unexpectedly, the cloud is not spherically symmetric.
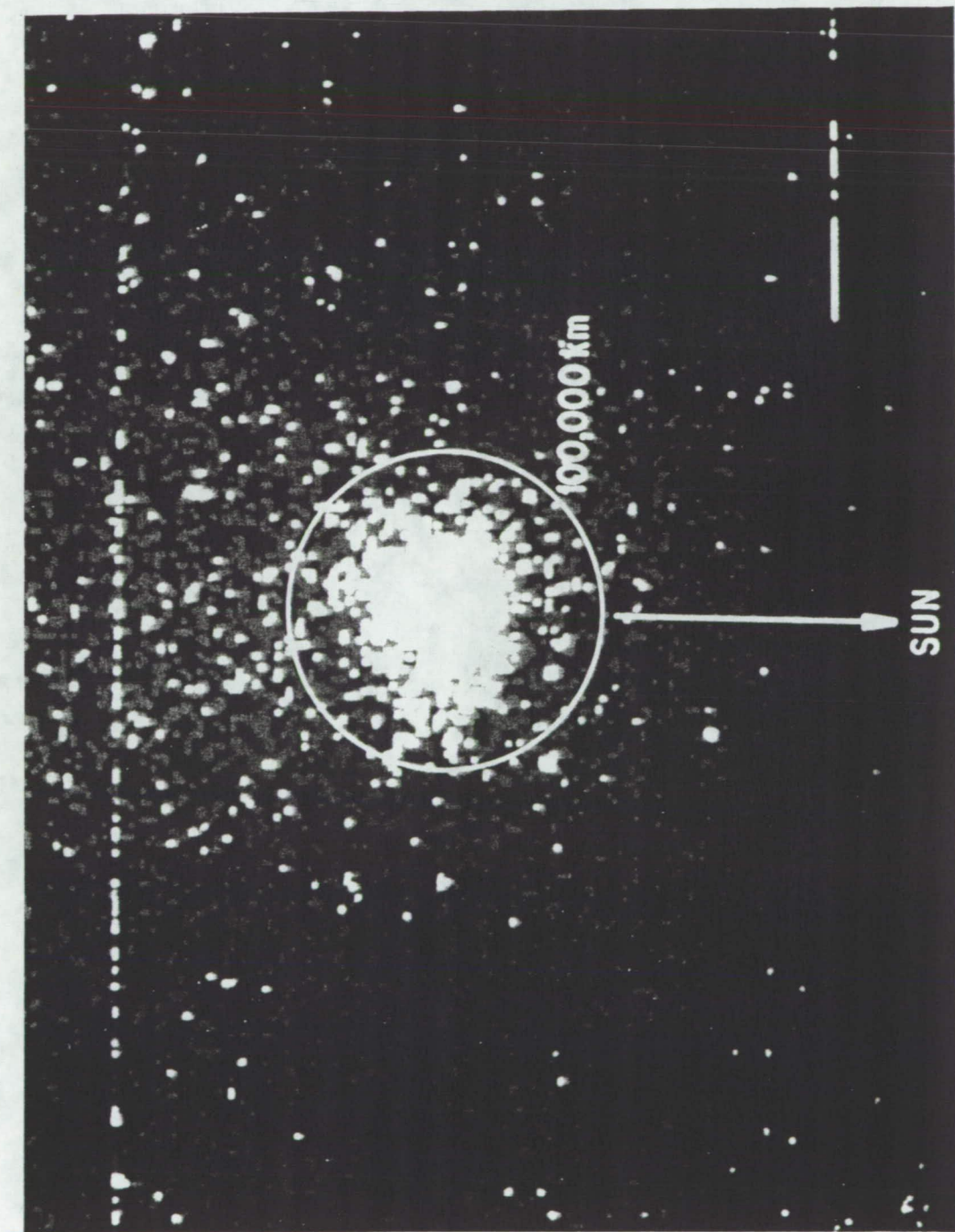
Figure 5. Image of Halley's Comet in the light of OI (6300 Å) emission made using a Fabry-Perot interferometer and an intensified CCD. The system sensitivity is about 36 R–S.

The information contained in the image is the subject of interest here, rather than the physics of the emission, which has been discussed elsewhere. The image was acquired with a 60-second exposure. The format of the array was 576x384 (0.022 mm) pixels which have been summed 2x2. The background level (dark noise) amounts to one photoevent in 10 pixels. Near the nucleus of the comet the signal is about 1 event per pixel. In spite of the low signal, the image shows an obvious change in surface brightness through one order of magnitude. The intensity near the nucleus was 6.3 R. The threshold is therefore about 0.6 R. Since this threshold was reached in 60 seconds, the sensitivity of the system was 36 R-s. This is consistent with the f/1 example above when we note that the ICCD was fed through a Nikon f/2 lens of focal length 135 mm. Through the 2x2 summation the effective pixel area was increased by a factor of 4 but at f/2 the solid angle decreased by a factor of 4. A transmission of 50% would bring the observation into line with the example.

There are other points that can be made from this demonstration. First we invite the reader to consider the various techniques which could be used in the data analysis and data collection to address this type of imaging. We will not discuss the data further. The question of the comparison of the ICCD image to the CCD image is important for completeness. In the discussion of the CCD it was estimated that 50 e^- would be required per pixel to give a S/N of unity. With the optical system used for the comet observation, the threshold intensity would have been 500 times higher. Even if the CCD noise level were 10 e^-, the threshold is still out of range by 100. Other optimization of the CCD is possible but we must also begin to consider such complicating features as working with limited charge and cosmic ray events, etc. We conclude that the strength of the ICCD lies in its application to aeronomical problems in which photons are limited.

References

C. D. Anger, S. K. Babey, A. L. Broadfoot, R. G. Brown, L. L. Cogger, T. Gattinger, J. W. Haslett, R. A. King, D. J. McEwen, J. S. Murphree, E. H. Richardson, B. R. Sandel, K. Smith, and A. V. Jones, "An Ultraviolet Auroral Imager for the Viking Spacecraft," Geophys. Res. Let. 14, 387-390 (1987).

R. Bredthauer, C. Chandler, J. Janesick, T. McDurnin and G. Simms, "Recent CCD Technology Developments," Instrumentation for Ground-Based Optical Astronomy--Present and Future, L. Robinson ed., Springer-Verlag, p. 486-492 (1988).

A. L. Broadfoot and K. R. Kendall, "The Airglow Spectrum, 3100-10,000 Å," J. Geophys. Res. 73, 426-428 (1968).

A. L. Broadfoot and B. R. Sandel, "Self-scanned Anode Array with a Microchannel Plate Electron Multiplier: the SSANACON," Applied Optics 16, 1533-1537 (1977).

A. L. Broadfoot, B. R. Sandel, D. E. Shemansky, S. K. Atreya, T. M. Donahue, H. W. Moos, J. L. Bertaux, J. E. Blamont, J. M. Ajello, D. F. Strobel, J. C. McConnell, A. Dalgarno, R. Goody, M. B. McElroy, and Y. L. Yung, "Ultraviolet Spectrometer Experiment for the Voyager Mission," Space Sci. Rev. 21, 183-205 (1977).

A. L. Broadfoot, B. R. Sandel, D. Knecht, R. Viereck, and E. Murad, "A Panchromatic Spectrograph with Supporting Monochromatic Imagers," submitted to Applied Optics.

H. Ebert, Wied. Ann 38, 489 (1989).

R. W. Engstrom, "Multiplier Photo-Tube Characteristic: Application to Low Light Levels," JOSA Vol. 37, 420 (1947).

W. G. Fastie, "A Small Plane Grating Monochromator," J. Opt. Soc. Am. 42, 641-647 (1952).

J. B. Holberg, "Far Ultraviolet Background Observations at High Galactic Latitude. II. Diffuse Emission," Ap. J. 311, 969-978 (1986).

J. R. Janesick et al., "The Future Scientific CCD," Proc. SPIE Vol. 501 (1985).

R. A. King, A. L. Broadfoot, B. R. Sandel, and A. V. Jones, "Correcting Image Distortion with Fiber-Optic Tapers," Applied Optics 27, 2048-2054 (1988).

M. L. Lampton, "Recent Advances in Detectors for the EUV," to appear in "Extreme Ultraviolet Astronomy," ed. R. F. Malina and S. Bowyer (New York, Pergamon Press).

K. Magee-Sauer, F. L. Roesler, F. Scherb, J. Harlander, and R. J. Oliversen, Spatial Distribution of O (^{1}D) from Comet Halley, Icarus, 76, 89 (1988).

G. R. Riegler and K. A. More, IEEE Trans. Nucl. Sci. NS-20, 102 (1973).

Rose, Weimer and Law, "The Image Orthicon--A sensitive Television Pickup Tube," Pub. I. R. E. Vol. 34, 424 (1946).

B. R. Sandel and A. L. Broadfoot, "Photoelectron Counting with an Image Intensifier Tube and a Self-scanned Photodiode Array," Applied Optics 15, 3111-3114 (1976).

O. H. Siegmund and R. F. Malina, ACS Symposium Series, No. 235, Vol. 2, 253 (1983).

J. G. Timothy, "Optical Detectors for Spectroscopy," Pub. of Astron. Soc. Pacific, 95, 810 (1983).

D. G. Torr, R. W. Basedow and G. H. Mount, Astrophysics and Space Science, 92, 237 (1983).

Figure 1. Signal-to-noise ratio ρ for CCD and ICCD detectors computed using equation 1. The straight line represents the ICCD, for which N is effectively zero because of the photo-electron counting capability of the ICCD. The curved lines represent CCD systems having readout noise of 10 and 50 electrons.

Figure 2. Comparison of a conventional Ebert-Fastie spectrometer with a spectrograph designed to take advantage of modern 2-dimensional detectors. In terms of the time required to cover the same range of wavelengths at equivalent resolution and statistical accuracy, the spectrograph has an advantage of a factor of 60.

Figure 3. Sensitivities for the instruments listed in Table 2. The letters labeling the lines match those in the table. The numbers show the number of spectral elements in each spectrum. The sensitivities of the monochromators depend on the number of spectral elements because of the necessity for time-sharing.

Figure 4. An illustration of the steps leading to a final spectrum from a spectrograph (after Holberg, 1986). Panel a: Raw spectra including signal and detector background. The detector background is due to intrinsic noise and to gamma rays from the radioisotope thermoelectric generators that power the spacecraft. Panel b: Result of subtracting detector background (top curve) and removing instrumental scattering (bottom curve). Panel c: Comparison of lower curve in panel b with a synthetic spectrum composed of He 584 Å and H Lyman series lines. Panel d: Residual after subtracting data and synthetic spectra in panel c.

Figure 5. Image of Halley's Comet in the light of OI (6300 Å) emission made using a Fabry-Perot interferometer and an intensified CCD. The system sensitivity is about 36 R-s.

A PANCHROMATIC SPECTROGRAPH

WITH SUPPORTING MONOCHROMATIC IMAGERS

A. L. Broadfoot and B. R. Sandel

Lunar and Planetary Laboratory

University of Arizona

Tucson, Arizona 85721

(602) 621-4301

D. Knecht, R. Viereck and E. Murad

Air Force Geophysics Laboratory

Hanscom Air Force Base

Bedford, Massachusetts 01731

(617) 377-3240

Abstract

The Arizona Imager/Spectrograph (AIS) is a set of imaging spectrographs and 2-D imagers for space flight. Nine nearly-identical spectrographs record wavelengths from 114 to 1090 nm with resolution of 0.5 to 1.3 nm. Spatial resolution along the slit is electronically selectable and can reach 192 elements. Twelve passband imagers cover wavelengths in the range 160 to 900 nm and have fields of view from 2° to 21°. The spectrographs and imagers rely on intensified charge coupled device detectors to achieve substantial capability in an instrument of minimum mass and size. By use of innovative coupling techniques, only two CCD's are required to record spectra from pairs of spectrographs. The fields of view of the spectrographs and imagers are coaligned, and all spectra and images can be exposed simultaneously. A scan platform can rotate the sensor head about two orthogonal axes. The AIS is designed for investigations of the interaction between the Space Shuttle and its environment. It is scheduled for flight on a Shuttle sub-satellite.
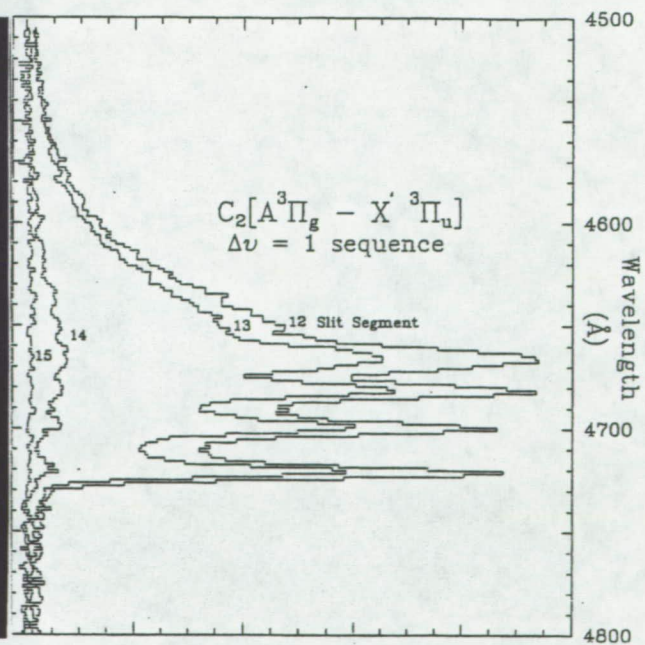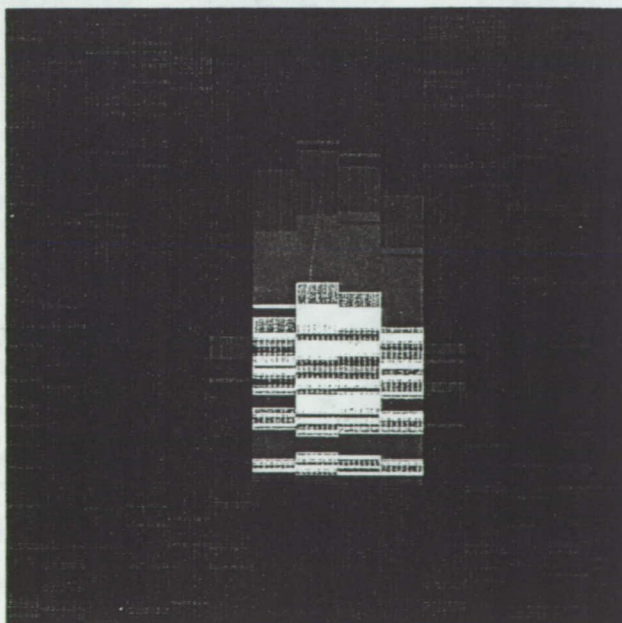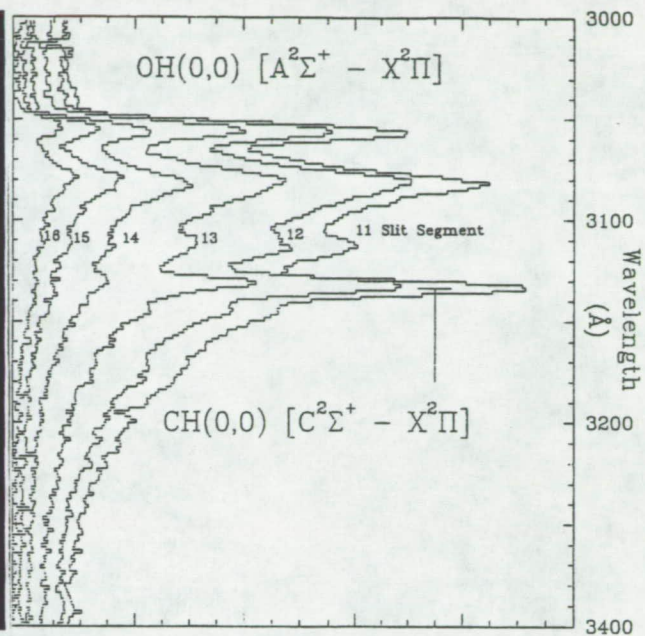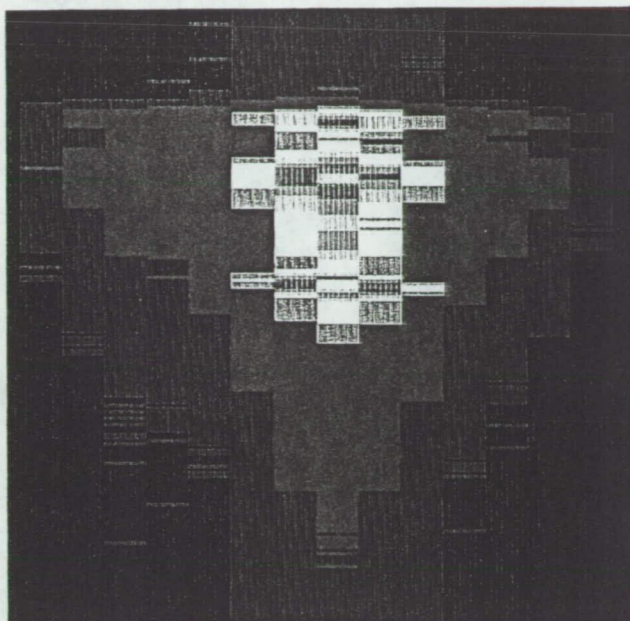
I. Introduction

The relationship between airglow observations and airglow models has always been a rather subjective one. Modeling now includes a remarkably extensive range of parameters, and present measurements do not effectively constrain all of them. Measurements of many parameters are required to evaluate and constrain the models. Unfortunately, the observations that are available for this purpose differ in important ways that complicate their intercomparison. They differ in time, air mass, altitude, solar flux, magnetic conditions, and excitation and quenching mechanisms. The assumptions in relating the data sets to each other are undoubtedly the main source of error so that the data set as a whole does not test a given model at its full potential. Applications of modern technology in optics, detector systems, electronic control and computing will make a revolutionary change in our ability to collect extensive data sets having fixed interrelationships. The instrument described here, the Arizona Imager/Spectrograph (AIS), is a starting point in attacking this problem.

The spectrograph has been recognized as an important diagnostic tool because it simultaneously records a large spectral passband and also retains spatial resolution along its slit. A detector having 2-D spatial resolution is required in the image plane; until recently that detector has been photographic film. Replacing the film by the intensified charge coupled device (ICCD) has improved our spectrographic capability in two important ways. First, the ICCD spectrograph has photon-counting sensitivity. Second, the size of the spectrograph is constrained by the detector size, which is quite small. The AIS exploits both of these advantages, while retaining spatial resolution along the slit. The application of ICCD's to airglow instruments is discussed in a companion paper (Broadfoot and Sandel, 1991).

An important guiding principle in the design, construction, and operation of the AIS has been to provide the capability for acquiring spectral and spatial information simultaneously. Toward that end, the spectrograph slit, which is imaged on the ICCD detector, is 2 pixels wide x 192 pixels long. The 192 pixels along the length may be summed into groups of a selectable number of pixels. Summing 8 pixels into each group (as in the example in Figure 1) divides the length of the slit into 24 segments, and separate spectra are recorded for each segment. Spatial inhomogeneities in the source will be represented in the set of spectra, which are recorded simultaneously. In this case, statistical accuracy in the spectrum is sacrificed to gain spatial information. Statistical accuracy in the spectrum can be recovered in data analysis by summing the adjacent segments, thereby sacrificing spatial detail to improve the signal to noise ratio of weak spectral features.

Figure 1 illustrates the advantages of this spectrographic technique. The flame of an acetylene torch was used as the target. In the schematic diagram in the right, the white line shows the projection of the spectrograph slit across the core of the flame. To the left is an enlarged view of the slit, showing that 20 of the 24 segments were illuminated by the flame. Aligned under the slit are the recorded spectra, one spectrum for each segment. Although the spectral range from 3000 Å to 9000 Å was recorded at the same resolution, we have selected two spectral regions that include two prominent bands for discussion. The color plot shows that the most intense emission originates in the center of

Figure 1. The spectral-spatial signature of an acetylene flame, illustrating the advantages of an imaging spectrograph, which records spatial variations in the spectrum of the source along the length of its slit. The schematic diagram at the upper right shows the location of the spectrograph slit projected on the flame. The field of view along the slit is divided into segments corresponding to different positions within the flame, as shown in the enlarged diagram to the left. Spectra recorded from the individual segments are shown in the color plots below the slit. The line plots are spectra from the selected segments indicated by the numbers near each line. This spatially-resolved spectrography reveals, for example, a difference in the spatial distributions of OH and CH emissions that would be difficult to measure by other means.

Flame Core

| 1 | 2 | 3 | 4 | 5 | 6 | 7 | 8 | 9 | 10 | 11 | 12 | 13 | 14 | 15 | 16 | 17 | 18 | 19 | 20 |

Slit (Spectral) Segments

OH(0,0) $[A^2\Sigma^+ - X^2\Pi]$

18 15 14 13 12 11 Slit Segment

CH(0,0) $[C^2\Sigma^+ - X^2\Pi]$

3000
3100
3200
3400

Wavelength (Å)

$C_2[A^3\Pi_g - X'^3\Pi_u]$
$\Delta\upsilon = 1$ sequence

15 14 13 12 Slit Segment

4500
4600
4700
4800
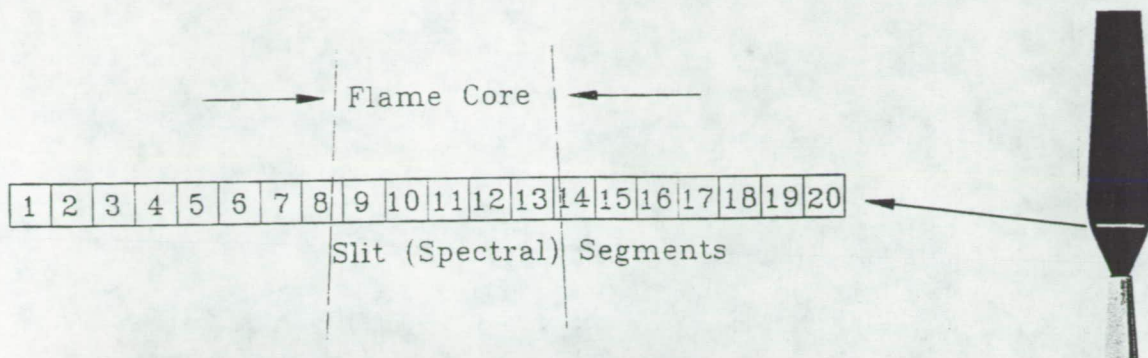
Wavelength (Å)

the core of the flame. The ultraviolet OH emission extends across 14 segments of the slit, while the longer wavelength C_2 (Swan) bands appear to be confined to the central core. It is noteworthy that the CH(0,0) band is more confined than the OH bands.

The spectrum of best signal to noise ratio will be obtained by summing the central four or five segments. Summing all the segments would increase the noise content unless the emission of interest filled the slit. An improved spatial signature for the band emissions can be obtained by summing the appropriate wavelength bins in the spectral direction.

A companion imager with a pass band near 3100 Å would show the extent of the OH emission in two dimensions, but only the spectrograph can separate the blended intensity profile of the CH emission from the nearby OH emission.

All of these techniques were available to us with the spectrograph and photographic plate. The improvement available now is in detector and electronic technology. We enjoy all of the attributes of the classical spectrograph combined with the photon-counting sensitivity of the photomultiplier for every pixel in the detector array.

This approach has a tremendous advantage in studying time-dependent phenomena, such as the active experiments, which have been performed to study ionospheric electron holes (Yau et al., 1985; Bernhardt, 1987; Mendillo et al., 1987; Bernhardt et al., 1988a; Bernhardt et al., 1988b) and atmosphere-plume interactions (Murad et al., 1990; Broadfoot et al., to be published). For example, Mendillo et al., 1987, observed 630 nm radiation when the Space Shuttle's OMS engines were fired. The observation was made with a narrow-banded filter. It is reasonable to attribute the radiation to $O(^1D) \rightarrow O(^3P)$. Since the radiative lifetime, τ, of $O(^1D)$ is ~120 s, spectral information as a function of distance along the line of release can be very valuable in determining the morphology of this species.

An important factor leading to the consistency of a spectrographic data set is recording the entire spectrum at the same time from the same gas column with diagnostic resolution. The AIS comes close to achieving this goal. It records the spectrum from 114 nm to 1090 nm simultaneously.

The spectrum is sampled at 5000 contiguous spectral intervals. The AIS is a true spectrograph, maintaining spatial information along its entrance slit.

The AIS addresses another problem common to airglow and auroral spectroscopy, namely that of relating the location of the observed gas column to the region of the scene being analyzed. The AIS has a complement of twelve co-aligned imagers; ten of which are intensified. By use of passband filters, the AIS records the spatial extent and surface brightness of emissions. All images are shuttered at the same time as are the spectra.

The instrument described in this paper was designed to meet the needs of a space flight program directed at the analysis of the "shuttle glow" (Banks et al., 1983; Mende et al., 1983). Earth's airglow is the background against which the shuttle glow will be observed. Useful airglow and auroral observations will be made during the same flight opportunity. The AIS is one of a group of instruments which form the payload of the Infrared Background Signature Survey (IBSS) flight program. The experiments are to be flown on the German-built carrier *Shuttle Pallet Satellite* (SPAS) *II*, which is manifested for flight on STS-39 in April 1991.

We have prepared a second nearly identical instrument for ground-based airglow and auroral measurements. The spectrograph section covers only the wavelength region from 300 nm to 1100 nm. The imager passbands and fields of view are adaptable to the classical auroral and airglow emissions. A third instrument is in preparation for Hitchhiker Shuttle flight opportunities, with the first flight expected in 1992. The primary target will be shuttle glow, contamination and flow fields, as well as airglow and auroral emissions from the atmosphere. The data formats of all of these instruments are identical, thus simplifying the intercomparison of data sets. The data are recorded in a widely-used format, the Flexible Image Transport System (FITS). The Image Reduction and Analysis Facility (IRAF) processing software developed by the Kitt Peak National Observatory will be used for data analysis.

II. Arizona Imager/Spectrograph Overview

The AIS spectrographs and imagers are mounted on an azimuth/elevation scan platform driven by stepping motors (Figure 2). The central box of the spectrograph/imager assembly includes five spectrograph housings of identical mechanical design. The spectrographs cover the wavelength range from 114 nm to 1090 nm in 9 overlapping wavelength bands. Pairs of double gratings in four of the spectrograph housings image 8 spectral bands onto four intensified CCD arrays. The fifth spectrograph housing contains a single grating and records the wavelength range from 900 nm to 1090 nm on a "bare" (unintensified) CCD. The field of view of the spectrographs is typically 0.2° x 2°. There are no moving parts in the spectrographs. Exposure is controlled electronically by a cathode gate potential or by using the high-speed CCD readout capability, 50 msec/frame. The characteristics of each spectrograph are given in Table 1.

Figure 2 also shows the cluster of twelve imagers. The imager baffles and intensifiers are mounted on top of the spectrographs. Flexible fiber optic image conduits carry the images to two CCD's mounted beneath the spectrographs. Ten of the images are intensified and two (the IR images) are not. The IR images are conducted directly to the CCD's by the fiber optics. These two IR imagers can accommodate bright signals and are used for accurate pointing (2° FOV) and field monitoring (18° FOV) to warn of bright emissions coming into the imaging space. Eight UV images are recorded with various passbands and fields of view to support the primary spectrographic experiment. The remaining two imagers have fields of view of 5° and are intensified and filtered for the visible wavelengths of the shuttle glow. The flexible fiber optic conduits have separate bundles to acquire the images from the image planes or from the fiber optic output of the intensifiers. At the CCD end, the fiber bundles are gathered in a 2 x 3 matrix which matches the image section of the CCD. The CCD is used in the frame transfer mode; the images are moved quickly from the image half to the storage half of the CCD, effectively shuttering the image. All functions are under microprocessor control.

Table 1. Spectrograph Characteristics

Spectrograph Designation	Wavelength Range (nm)	Resolution (nm)	Photosensitive Material	Dispersion (nm/pix)	Quant. Eff.	F-Ratio	Sensitivity (dn/sec) per Rayleigh
1	1090 - 900	1.3	Si*	0.32	0.1	2.9	0.003
2	930 - 764	0.9	GaAs	0.29	0.18	4.1	1.4
3	774 - 608	0.9		0.29	0.18	4.1	0.8
4	617 - 532	0.45	S-20	0.15	0.12	4.1	0.7
5	548 - 462	0.45		0.15	0.12	4.1	1.25
6	468 - 382	0.45	S-20	0.15	0.25	4.1	0.3
7	386 - 300	0.45		0.15	0.25	4.1	0.7
8	302 - 200	0.54	Cs_2Te	0.18	0.06	4.1	0.3
9	220 - 114	0.54		0.18	0.05	4.1	0.3

* Unintensified

VIEW
DIRECTION

ELEVATION

SIDE VIEW
ELEVATION = 30°

← 56 cm →

AZIMUTH

IMAGERS | SPECTROGRAPHS

CCD'S FOR
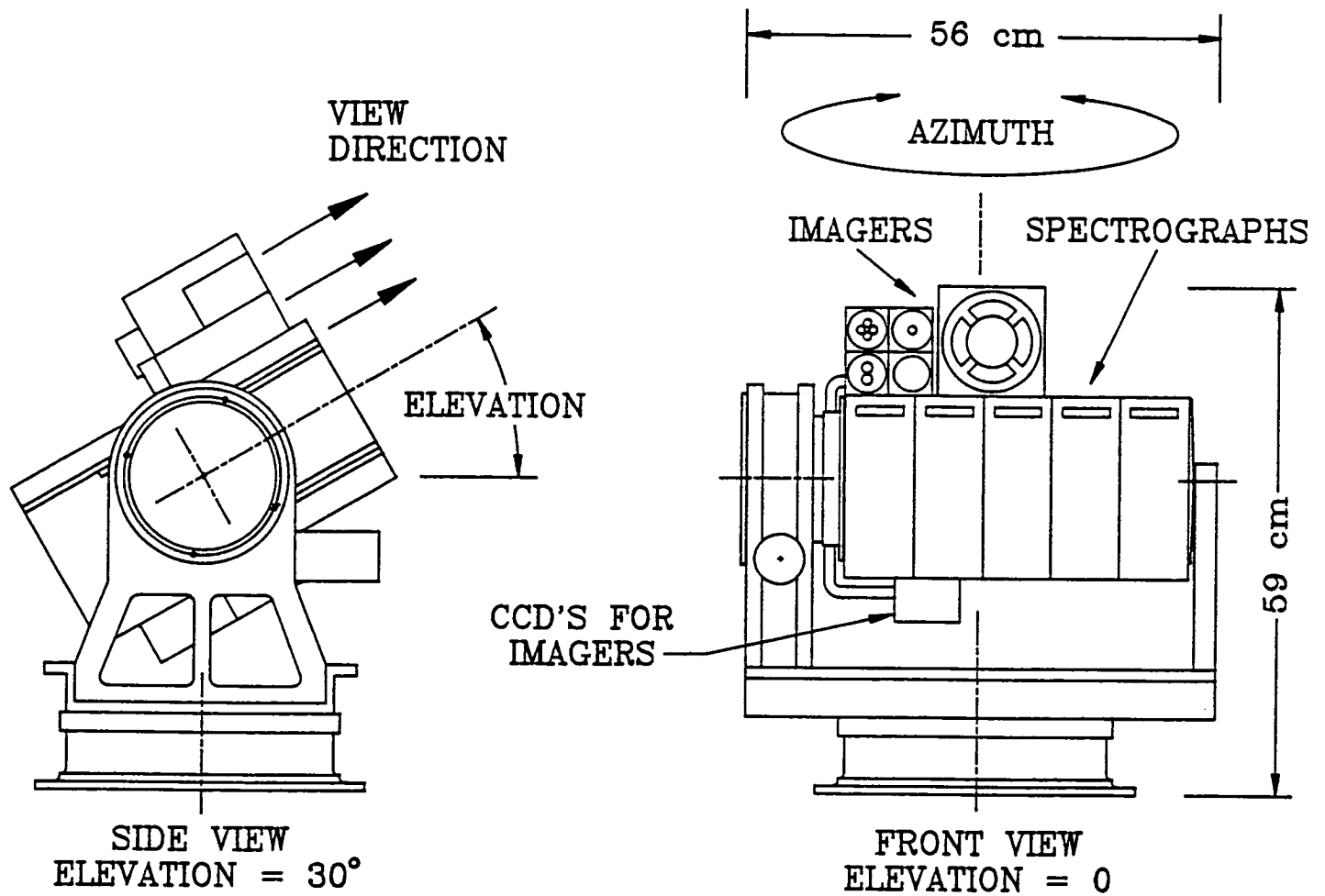IMAGERS

59 cm

FRONT VIEW
ELEVATION = 0

Figure 2. Two views of the AIS spectrographs and imagers mounted on their scan platform. The nine spectrographs are separated into five housings. Above the spectrograph housings are the twelve passband imagers. The axes of rotation pass through the center of gravity of the rotating section. The fields of view of all the spectrographs and imagers are co-aligned.
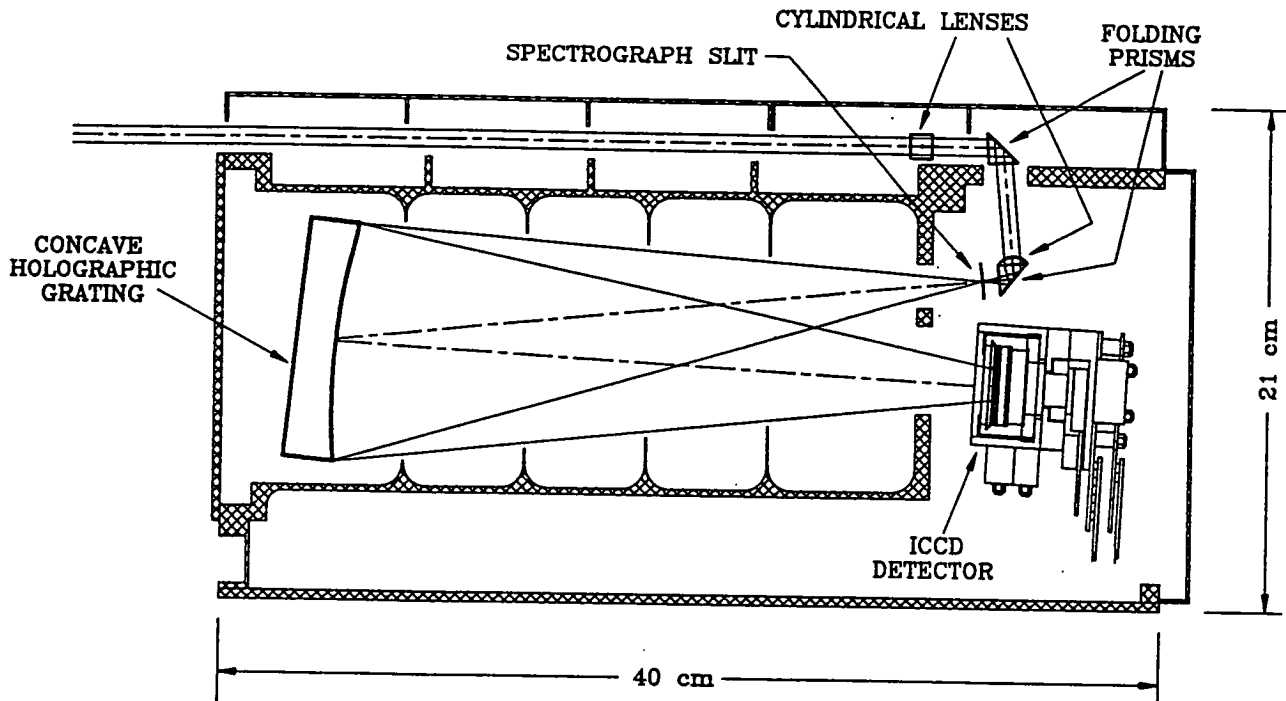
Figure 3. A cross-section in the plane of dispersion of one of the spectrographs. All the spectrographs are based on concave holographic aberration-corrected gratings, and hence have a common design. Cylindrical lenses improve baffling and minimize the size of the fore-optics.
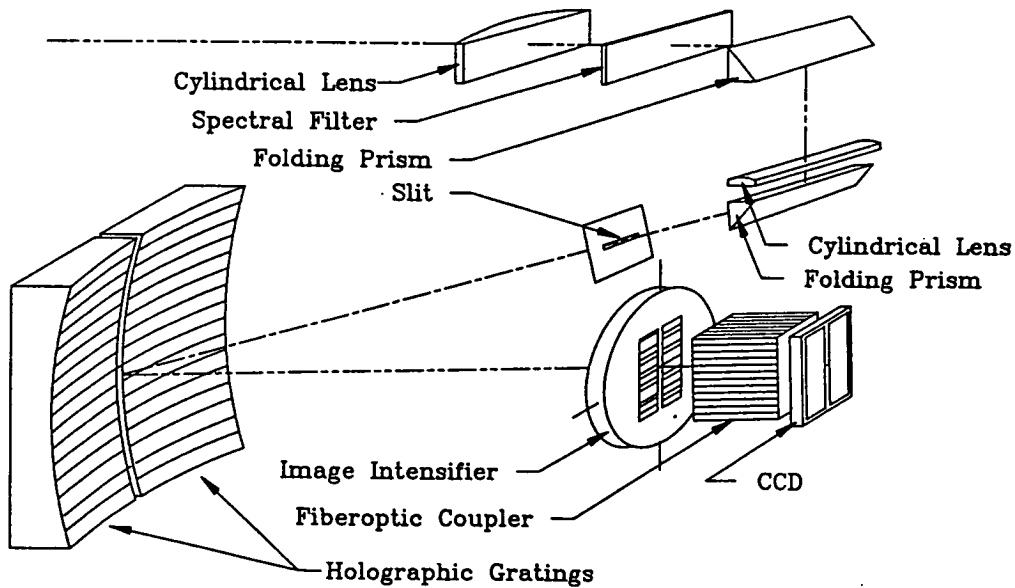

Figure 4. Schematic diagram of a dual-grating spectrograph. Each grating images its dispersed spectrum on one half of the rectangular detector. A single slit feeds both gratings.

III. Imaging Spectrographs for ICCD Detectors

A. Spectrograph Optics

Figures 3 and 4 show the primary features of the optics. After reviewing several optical designs for usefulness with the ICCD detector, we chose one employing aberration-corrected holographic concave gratings. The simplicity of the mechanical design, which could be used at all wavelengths, 20 to 1100 nm, was the strongest argument. This design requires only one optical element and one surface, compared to 5 optical elements and 9 surfaces required by an alternative classical design. The gratings were designed by American Holographics, Inc. Although the first set was expensive, successive sets were very economical. Tables 2 and 3 summarize grating characteristics and spectrograph design parameters.

The number of spectrographs and gratings required to cover the wavelength range from 114 nm to 1090 nm was determined primarily by the spectral dispersion required for a diagnostic spectrum. At short wavelengths, the airglow spectrum is fine-structured and requires about 0.3 - 0.5 nm spectral half-width to separate blends and determine rotational structure in molecular bands when accurate spectral modeling is used. At the longer wavelength end of the spectrum, band systems are broader, reducing the dispersion requirement somewhat. The length of the CCD array and the pixel size determine the "plate" dispersion. For a spectrograph the ideal transmission function is rectangular and two pixels in width; therefore the 576-pixel array can record 288 spectral elements along its length, or about 100 nm for a 0.3 nm width. Secondary constraints included the separation caused by the photocathode response and the goal of reasonably small size. With these constraints, the spectrum from 114 nm to 1090 nm was divided into nine overlapping bands (Table 1). Although it would be possible to build 9 identical spectrographs to cover the spectral range, such a unit would be too large for a practical flight instrument. By using two gratings in each spectrograph we achieved a tractable instrument size. Reducing the grating area results in a loss in through-put by a factor of 2. By reducing the slit length to allow the two spectra to be recorded side by side on a single CCD,

the detector area is also reduced by a factor of 2 (Figure 5). The accumulated reduction in throughput is therefore a factor of 4.

TABLE 2

GRATING CHARACTERISTICS

Grating Number	Wavelength Range (nm)	Slit to Grating Distance (mm)	Grating to Detector* Distance (mm)	Angle of Incidence (degrees)	Angle of Diffraction	Angle, Slit to Detector Center
1	1090–900	259.5	277.7	11.5	2.5	9.0
2	930–764	271.2	276.5	10.9	2.7	8.3
3	774–608	271.0	276.3	9.7	1.4	8.3
4	617–532	268.3	279.7	13.4	4.4	9.0
5	548–462	268.0	279.4	12.1	3.1	9.0
6	468–382	271.2	277.0	10.2	2.7	7.5
7	386–300	271.0	276.8	9.0	1.5	7.5
8	302–200					
9	220–114					

*The spectral plane is perpendicular to the line between grating center and detector center.

TABLE 3

SPECTROGRAPH DESIGN PARAMETERS

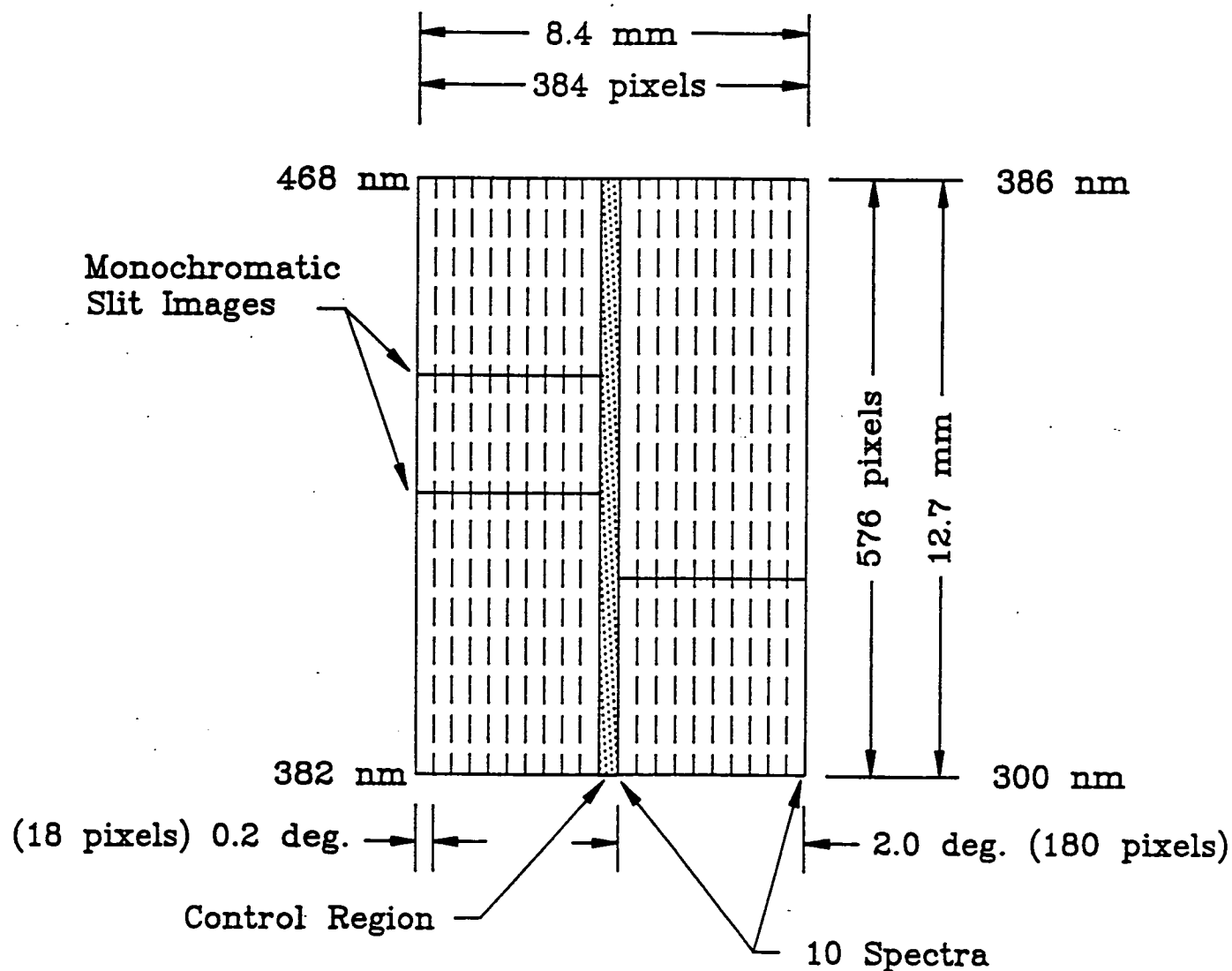| INSTRUMENT PARAMETERS	Dual Grating	Single Grating
Full Pixel Array (per spectrum)	180 x 576	360 x 576
Element Size (monochromatic slit image, mm)	180 x 2	360 x 2
Grating Radius of Curvature (mm)	275	275
Slit Dimensions (mm)	0.04 x 4.0	0.04 x 8.0
Grating Dimensions (mm)	35 x 100	70 x 100
Effective f/number	4.1	2.9

Figure 5. The organization of the two spectra dispersed onto one ICCD. Readout proceeds by shifting the charges in the top row of pixels horizontally and digitizing them one by one; the charge on all pixels is then shifted vertically by one row. This sequence is repeated until the charge collected on all pixels has been sampled serially. The charge from more than one pixel can be shifted into the output capacitor resulting in "on chip charge summation." Typically several pixels are summed horizontally (the direction parallel to the slit). The readout pattern in computer controlled.

Spectrograph 1 is an exception. The photoelectric sensitivity in the 900-1090 nm range is comparatively low for either of the possible detectors, bare silicon of the CCD or the S1 (cesium) photocathode. The bare CCD was selected because the S1 photocathode requires special cooling which might not be available and the sensitivities are not much different. For this spectrograph we chose a lower dispersion to allow a single grating to be used for optimum throughput.

The position of the ICCD detector was unique for each spectrograph. The optical design required that the grating-slit distance be common for all spectrographs and that the detector be perpendicular to the line from the grating center to the detector center. This condition places all the variability in the 5 spectrographs in the detector position. A special coupler was designed for each spectrograph to satisfy these optical design requirements.

B. Foreoptics

The field of view of the spectrographs was specified to be 2.3° to encompass the scale of emissions at the expected range to the target. Since the spectrograph slit was 4 mm long, a 100 mm focal length was required. A single lens could be used but the diameter would have been 50 mm and a sizable baffle system would be required. Instead, cylindrical optics were used to simplify the baffling and minimize the volume of the optical enclosure .

The folded refractive optical system is shown in Figures 3 and 4 and in the more detailed Figure 6. Internal reflection in a prism serves as the folding element to minimize reflective losses. A ray trace showed that some of the rays striking the slit prism would not be internally reflected, so the back surfaces of these prisms were silvered. Crossed cylindrical lenses image the target on the slit. A cylindrical lens of 19 mm focal length is located 19 mm from the slit. The slit width of 0.045 mm restricted the angular width of the field of view to 0.14° outward from the lens. The width of the grating acceptance angle through the slit at the lens was 7 mm. The second cylindrical lens, of 100 mm focal length, is located 100 mm from the slit where the cross sectional area of the projected grating acceptance angle is about 7.2 mm x 30 mm. The cross sectional area at entry to the baffle is 7.4 mm x 32.2 mm.

Cylindrical Lens

Prism (Total Internal Reflection)

Cylindrical Lens
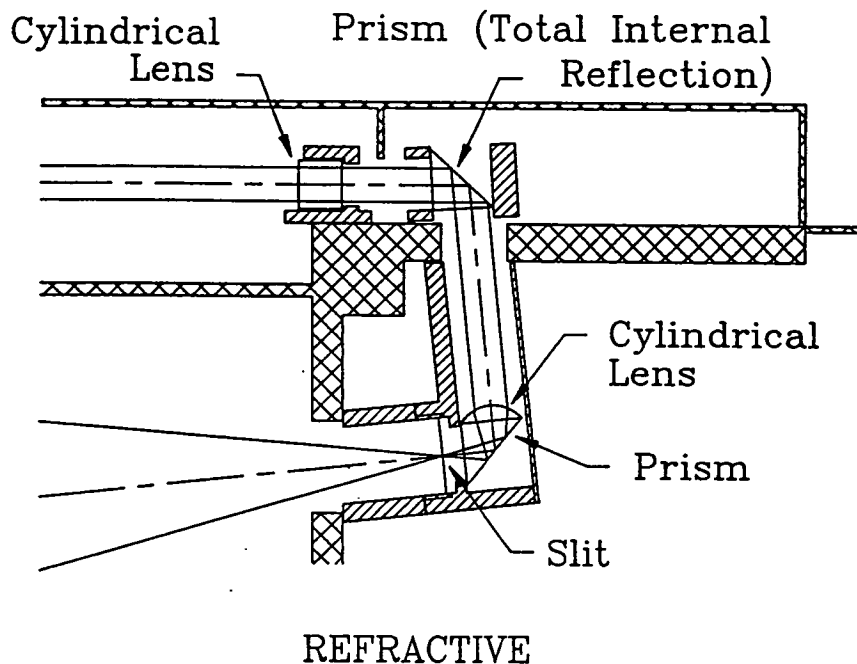
Prism

Slit

REFRACTIVE

Figure 6.   A cross-section of the refractive fore-optics used for all but the UV spectrograph. The fields of view across and along the slit are controlled separately with crossed cylindrical optics.

Cylindrical Mirror

Folding Plane Mirror

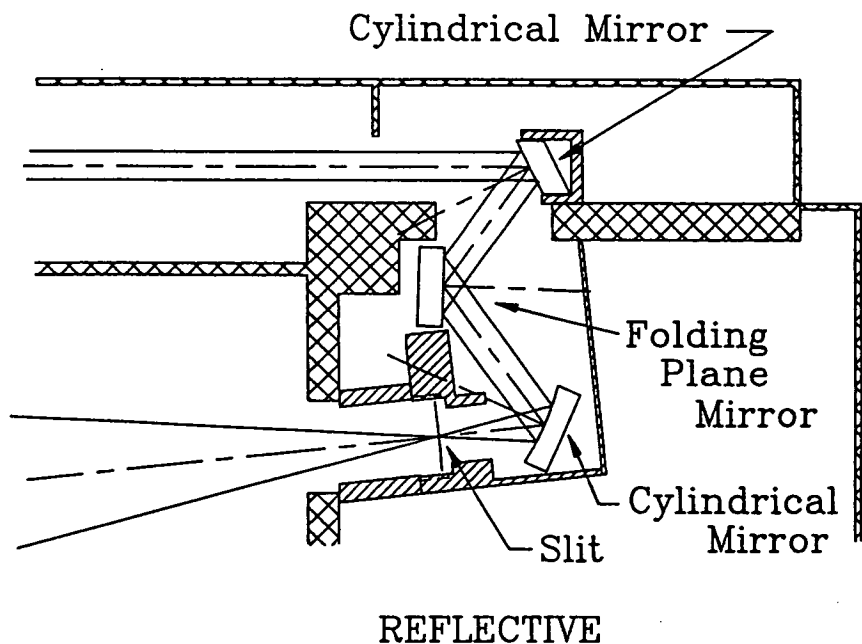Cylindrical Mirror

Slit

REFLECTIVE

Figure 7.   A cross-section through the reflective fore-optics of the UV (115 nm - 320 nm) spectrograph.   The refractive optics of Figure 5 were replaced with the equivalent cylindrical reflective components.   Considerable spherical aberration in the FOV was introduced but will not reduce the data quality.

Two spectrographs required special attention. Spectrograph #1 has an entrance slit 8 mm long and therefore requires a focal length of 200 mm to match the field of view of the other spectrographs. The addition of a concave 25 mm focal length cylindrical lens and adjustment of the position of the 100 mm lens resulted in an effective focal length of 200 mm. Reflective cylindrical foreoptics were needed for spectrograph 5, which covers the wavelength range from 115 to 320 nm (Figure 7). Although the problem of chromatic aberration in refractive optics was eliminated, considerable spherical aberration was introduced by the short focal length cylindrical surface. Three reflections were required to match the field of view requirements. The reflective surfaces were coated to enhance UV reflection to 1150 Å.

C. Thermal Compensation

For most satisfactory performance the CCD's and intensifiers should be at a temperature below -10 C. At these temperatures both the CCD leakage current and intensifier shot noise will be small during an exposure time of 10 seconds. To achieve this temperature the whole spectrograph is radiatively cooled. Alignment is done at room temperature, and the SPAS flight thermal model predicts temperatures as low as -70 C. This is a temperature range of 100 C, implying a change of about 0.07 cm in length of the spectrograph body over the focal length of 27.5 cm due to thermal contraction. A change in focus of only 0.012 cm would degrade the spectral resolution. Therefore the grating-detector separation is thermally compensated by the mechanical design and material selection. The gratings in the spectrograph are deposited on Zerodur blanks which has a coefficient of thermal expansion near zero. To maintain focus through the temperature extreme the position of the grating relative to the slit and detector is established by invar rods which are 29.2 cm long between clamps, which limits the change in focus to 1×10^{-3} cm for $\Delta T = 100$ C. A stainless steel diaphragm is sandwiched in the grating holder and attached to the spectrograph frame. This diaphragm provides lateral support of the grating but deforms to allow longitudinal motion. Invar rods extend from the four corners of the grating holder to fixed points near the image plane as noted above.

IV. Passband Imagers

A. Airglow Imaging

The main purpose of imaging in this investigation is to provide information about the spatial distributions of a variety of species. It is also designed to allow pointing of the spectrographs accurately and provide a photometric map of extended gas clouds which are being analyzed by the spectrographs; therefore high spatial resolution is not necessary. Imaging must be done simultaneously to properly associate the bandpass images to changing conditions and to be contemporaneous with the one dimensional image of the spectrograph (Broadfoot and Sandel, 1991). For this reason we use multiple imagers instead of a filter wheel. The CCD image frame of 384 x 288 pixels was subdivided into 6 arrays of 128 x 144 pixels (Figure 8). With two CCD's, we expose 12 images simultaneously. Flexible fiber optic image conduits collect the images directly or from intensifiers and transfer them to the CCD's.

Because of the small image format (2.8 mm x 3.2 mm), miniature optics can be used, and up to 6 images can be formed on a single standard 18 mm image intensifier. Broadfoot and Sandel (this issue) point out that the photometric efficiency (E) of an imager is independent of the size of the imager since the throughput is proportional to the detector area (A) and the solid angle of illumination (Ω) where the solid angle Ω is in turn proportional to the reciprocal f-ratio squared. That is, $E \propto A/f^2$. The area of the detector is the pixel which is a constant of the system. The f-ratio is independent of the size of the optics. The design parameter remaining is to satisfy the field of view by selection of the focal length, then optimize the aperture to minimize the f-ratio.

B. The Imager Set

Figure 8 summarizes the imager sets. The sets are classified as narrow angle (N) or wide angle (W) and referred to the wavelength regions UV, VIS, and IR. Images formed by the lenses are conducted by flexible fiberoptic bundles to two CCD's. The two IR imagers are not intensified. Proximity focused image intensifiers are used to intensify the remaining 10 images. The light from the phosphor is conducted by the fiberoptic faceplate to a flexible fiberoptic image conduit. The light

Table 4. AIS Imager Characteristics.

| Imager Number	Imager Type	Imager Designation	Wavelength peak (hw) (nm)	Angular FOV Az	El	Photo-sensitive Material	Angular Resolution (deg/pix)	Quantum Eff. (% trans.)	F-Ratio	Sensitivity (dn/sec) per Rayleigh per pixel
1	Narrow-UV	NUV 160	160 (25)	1.8°	1.6°	Cs_2Te	0.013°	0.05	2.2	0.076
2	Narrow-UV	NUV 200	200 (25)	1.8°	1.6°		0.013°	0.06	2.2	0.070
3	Narrow-UV	NUV 235	235 (25)	1.8°	1.6°		0.013°	0.06	2.2	0.13
4	Narrow-UV	NUV 260	260 (25)	1.8°	1.6°		0.013°	0.06	2.2	0.39
5	Wide-UV	WUV 160	160 (25)	25°	21°	Cs_2Te	0.17°	0.05	2.2	0.58
6	Wide-UV	WUV 200	200 (25)	25°	21°		0.17°	0.06	2.2	0.55
7	Wide-UV	WUV 235	235 (25)	25°	21°		0.17°	0.06	2.2	0.65
8	Wide-UV	WUV 260	260 (25)	25°	21°		0.17°	0.06	2.2	1.6
9	Medium-Vis	VIS 500	500 (200)	6.0°	5.3°	S-20	0.042°	0.11	2.6	4.0
10	Medium-Vis	VIS 700	700 (200)	6.0°	5.3°		0.042°	0.09	2.6	2.3
11	Wide-IR	WIR 900	900 (400)	21°	19°	Si*	0.15°	0.1	2.3	0.098
12	Narrow-IR	NIR 900	900 (400)	2.3°	2.0°	Si*	0.016°	0.1	2.3	0.082

* unintensified CCD
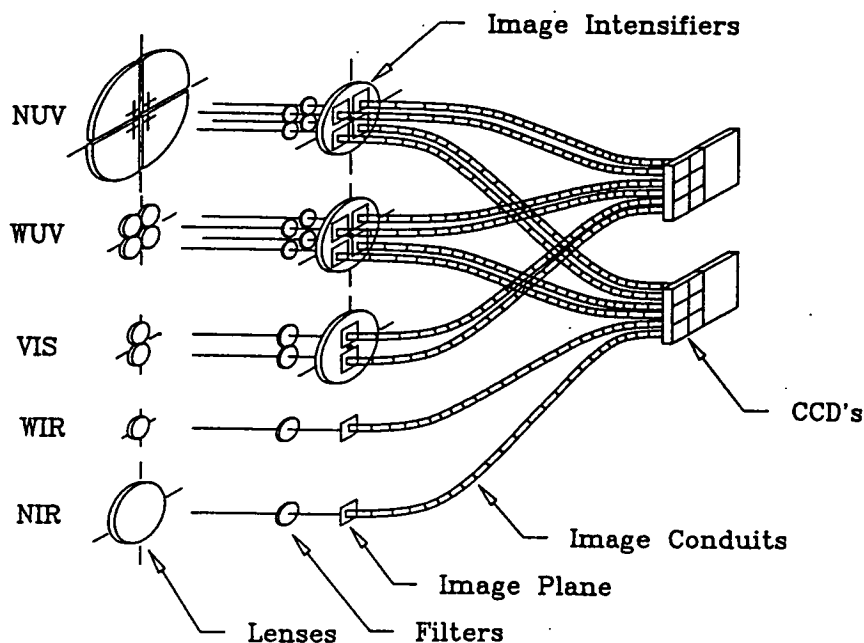
Figure 8. Schematic diagram of the imager components. Coherent fiber optic bundles transfer the passband images to one of two CCDs.
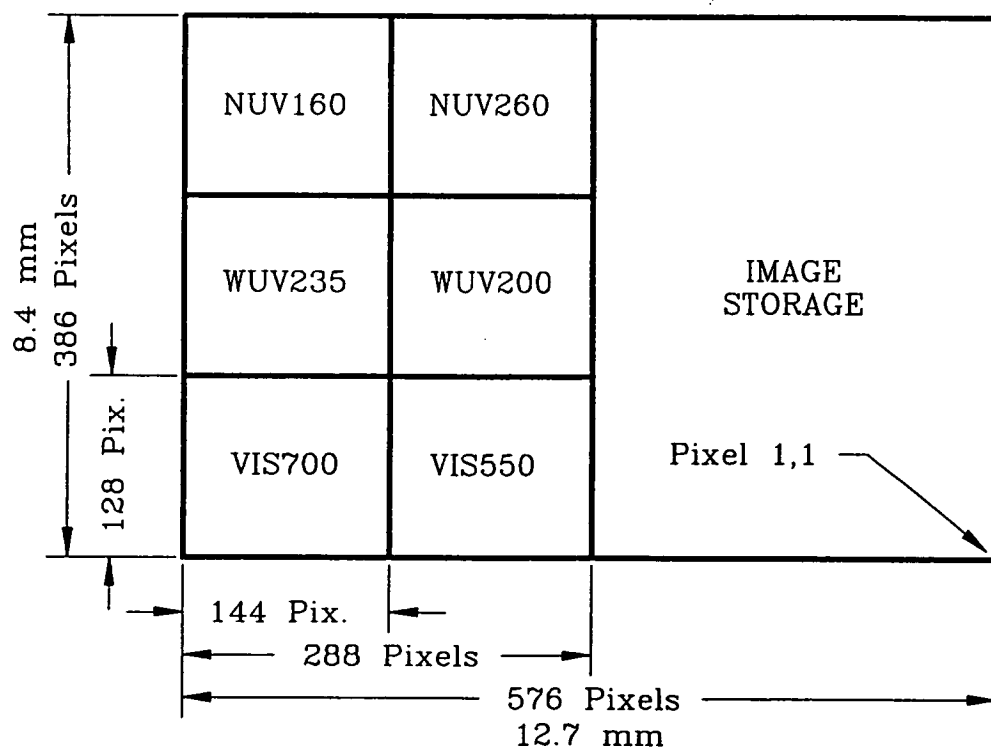

Figure 9. The locations of images on one of the two CCD's used for imaging. The frame transfer capability of the CCD is used to move the image to the storage area. Exposure continues while the storage area is being digitized. The second imaging CCD records the remaining six images in a similar way.

is conducted to a third fiberoptic window which is in contact with the surface of the CCD. The images were arranged in groups of six as illustrated in Figure 9 on the image half of the CCD. The UV images were split to minimize the effect of a failure in a single CCD. In retrospect, this arrangement was more complicated than needed; future instruments would not use such an arrangement.

The imager complement needed to satisfy the scientific requirements is listed in Table 4. Eight imagers record UV emission in 4 different passbands in the 150 nm to 270 nm wavelength range. Four of these have a field of view of about 2°, to match the spectrographs. The remaining four imagers have similar pass bands but 25° fields of view to examine the larger context of the spectrographs and narrow angle imagers.

Wide and narrow angle unintensified imagers will assist in several ways. Their wavelength band is restricted to the IR region around 900 nm, which will probably be an important region for shuttle glow. The narrow angle (2° field of view) imager will define the pointing of the spectrographs. The wide angle (18° field of view) imager will survey the field and detect bright sources which should be avoided by the intensified channels. The shuttle glow is also the target of interest for the other two medium field (5° field of view) imagers that cover two visible bands.

C. IR Imagers

The IR imagers are the most straightforward since the image is formed directly on the end of the flexible fiberoptic bundle. The lens for the wide angle imager is a commercial lens of 9 mm focal length and 5 mm diameter lens. A filter between the lens and the fiber bundle limits the wavelength to > 700 nm. Lens and filter are located in the center of a plate spaced from the image plane to focus. Figure 10 illustrates the mechanical layout. A standard frame size of 50 mm square was used for most of the imagers' sections. The insides of the baffle tubes were machined to a common diameter so that baffles and spacers for most imagers have a common outside diameter. Inside diameters of the baffles were machined in a jig, which allowed all baffle sets to be machined as a group and provide tapered

knife edges. The baffles and spacers were stacked in the baffle tube and held in by a jam nut. The walls of the baffle tubes were machined to leave a wall thickness of 1.3 mm between square endplates.

Figure 11 is a section through the narrow angle IR imager. A lens with a 75 mm focal length and 40 mm diameter was selected for this application. In both IR imagers the end of the fiberoptic bundle can be moved to adjust the focus.

D. Visible wavelength imagers

Figure 12 is a cross-section through the two visible imagers. Two identical lenses (focal length, 35 mm; diameter, 9mm) form separate images on the photocathode of a single proximity focused image intensifier. The fiberoptic output of the intensifier is coupled to the flexible fiberoptic bundle to transfer the image to the CCD.

E. Wide angle UV imagers

The wide angle UV images presented some special problems. Given the chosen image size, the desired field of 25° implies a focal length of 6.8 mm. Using such a short focal length lens was complicated by the fact that the intensifier window was 5 mm thick. Re-imaging designs using refractive spherical optics were considered, but they presented many problems and did not provide better imaging than the single lens used. The wide angle lens consists of a MgF_2 hemisphere and a MgF_2 spacer form an image on the photocathode. An aperture stop at the base of the hemisphere limits image aberrations. Ray tracing showed significant changes in the imaging properties from center to edge of the image plane due to the change in focal distance. The two adjustable parameters were the size of the aperture stop and the focal plane distance. It was demonstrated that fairly uniform image quality over the image plane could be achieved with an f/2 aperture stop and with the image plane at the median distance between best focus for on-axis and edge rays. Most (80%) of the rays fall inside a circle of diameter 2 pixels. This is acceptable resolution for an imager intended to detect changes in the surface brightness of extended gas clouds.

Figure 13 is a cross-section through two of the imagers. The proximity focused image intensifier has a MgF_2 window and Cs_2Te photocathode with a sensitive area 17 mm in diameter. The
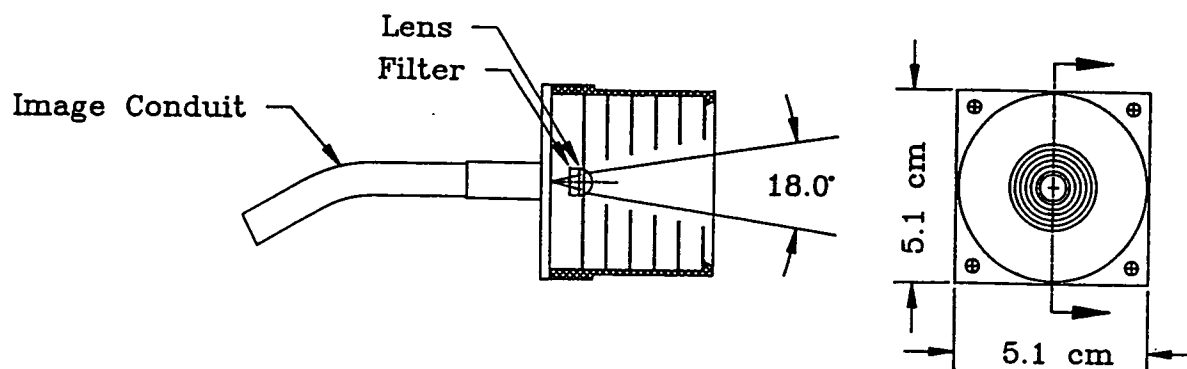
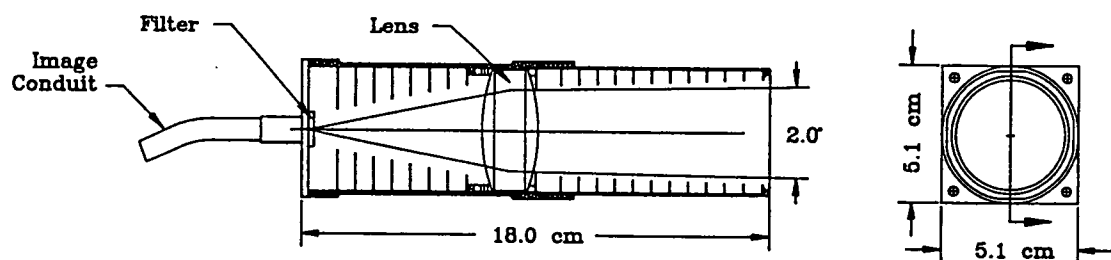Figure 10. The wide angle infrared imager (WIR). No image intensifier is used for this passband.

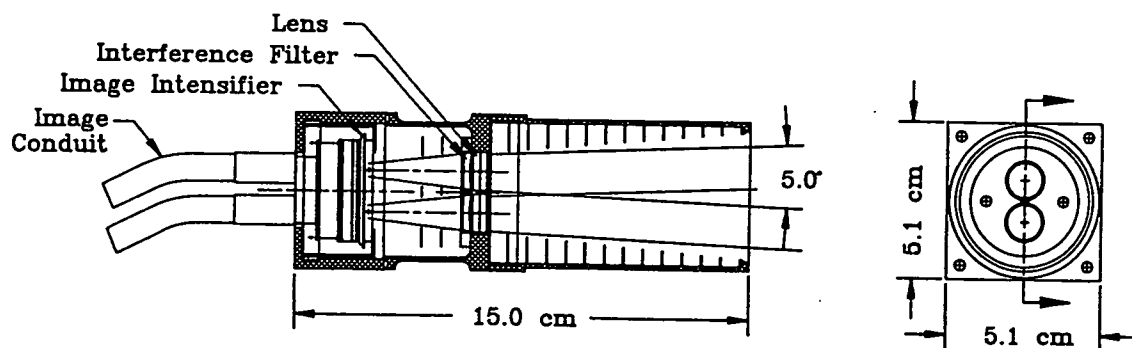Figure 11. The narrow angle infrared imager (NIR).

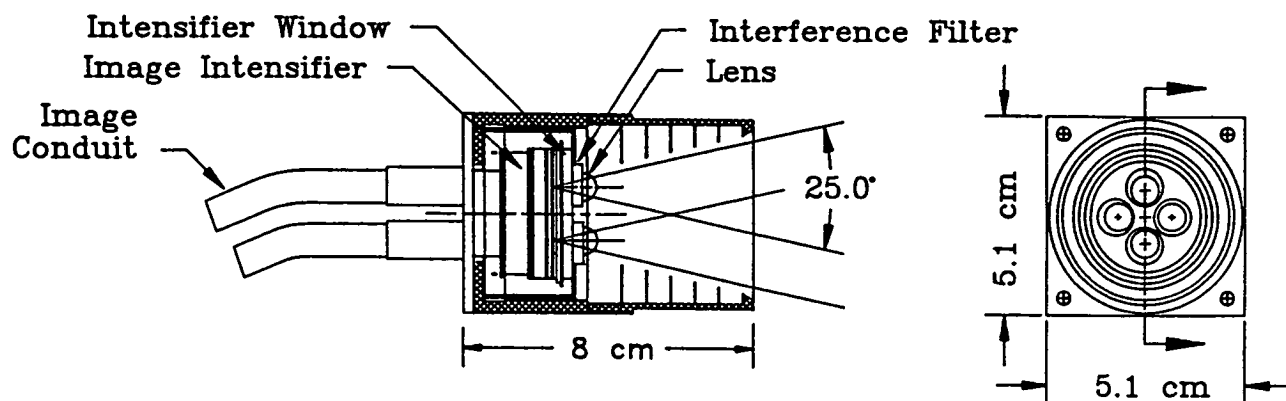Figure 12. The two visible intensified imagers (VIS 700, 500).

Figure 13. The set of four wide angle ultraviolet imagers (WUV 160, 200, 235, 260). Because of their short focal lengths, the four lenses are bonded to the window of the image intensifier.
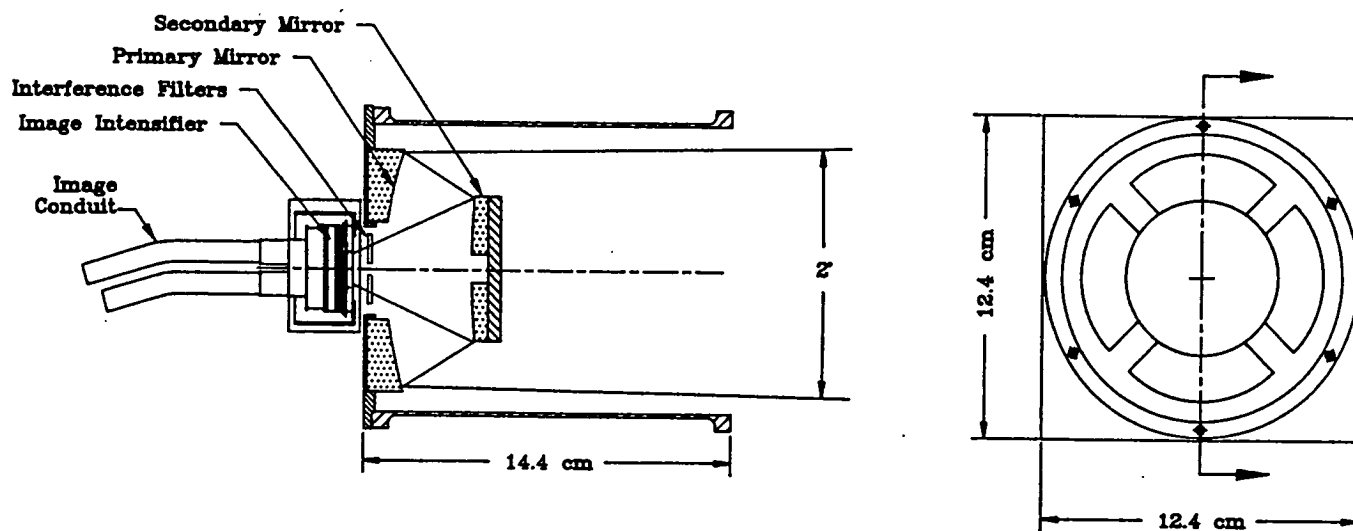

Figure 14. The set of four narrow angle ultraviolet imagers (NUV 160, 200, 235, 260). The cassegrain design uses a four-segment optical system to form separate images in each of four passbands.
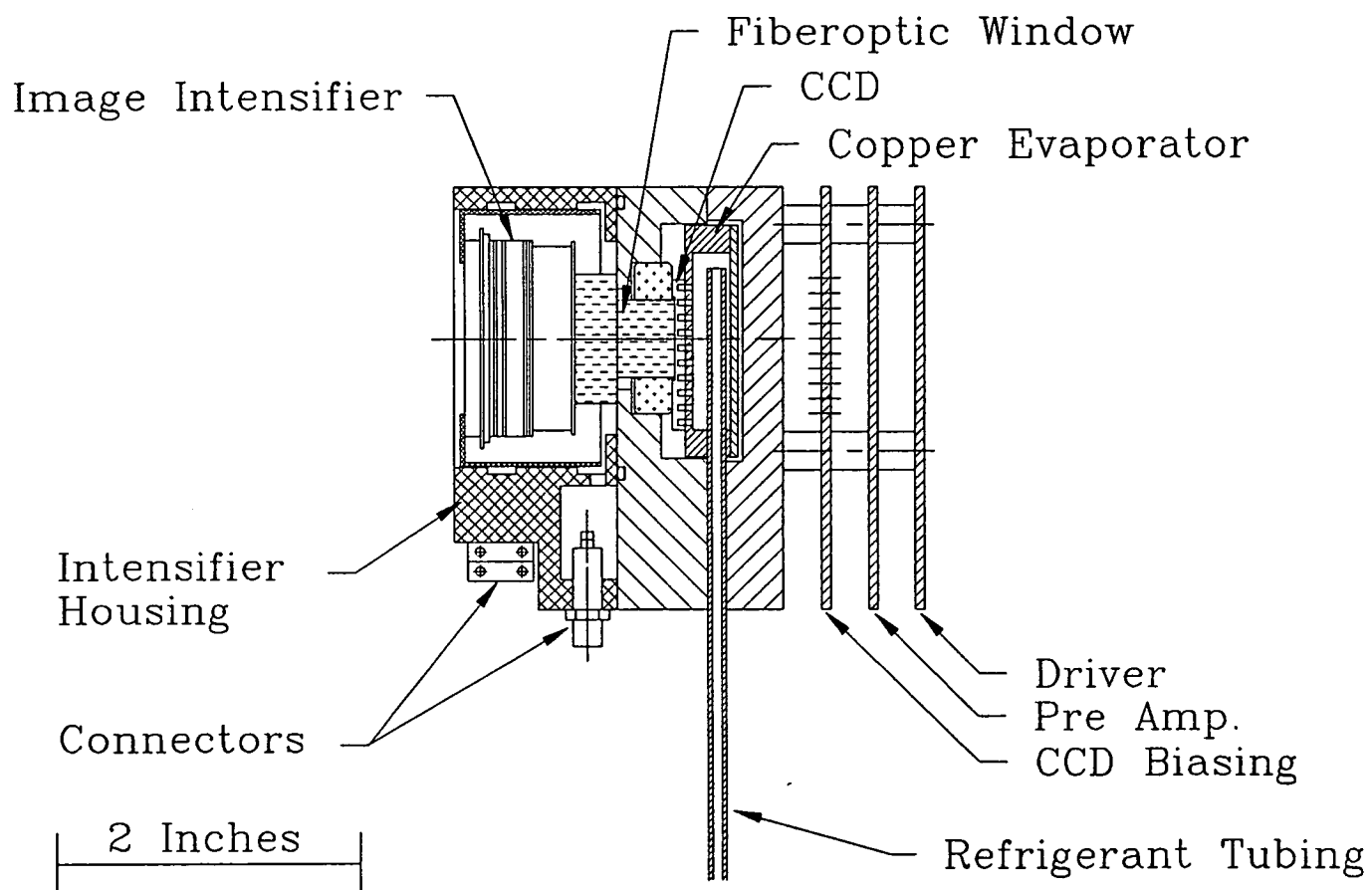
Figure 15. The intensifier-CCD assembly. The refrigeration evaporator is used only for laboratory testing. The AIS is passively cooled in flight.

center of the images lie on a circle 12.75 mm in diameter which is common to all of the multiple imagers.

F. Narrow angle UV imagers

The design goals for the narrow angle (2°) imager set were to achieve a minimum mass, using a single image intensifier, while maximizing the throughput and minimizing cost. A tradeoff study of both refractive and reflective optics was carried out in parallel with a search for commercially available lens systems. Refractive designs could be used, but would require changes for each wavelength. The reflective design seemed more general. A high-speed reflective optics lens manufactured by the Nye Optical Company appeared to have the best characteristics. It employs a spherical primary surface and an aspherical secondary in a Cassegrain configuration. The effective focal length is 90 mm and the effective focal ratio is 1.1.

Mechanical modifications of the selected lens were needed in order to have four optical axes and thereby four images. A cross-section of this imager is shown in Figure 14. The lens was sawed into 4 pie-shaped sections which were then separated by the appropriate distance, 12.75 mm as mentioned above. The secondary was re-assembled and bonded to a backplate of appropriate material. Provision was made to adjust the primary sections individually. Preliminary adjustments were made at visible wavelengths before the band pass filters and the Cs_2Te intensifier were installed.

V. Intensified CCD Detectors

Application of the intensified CCD detector has been discussed in detail in a companion paper (Broadfoot and Sandel, 1991). The principles outlined there have been used to define the AIS. Figure 15 shows an ICCD assembly.

Proximity-focused image intensifiers were procured from several manufacturers. Four cathode materials were used to cover the spectrum (Tables 1 and 4). Two special specifications were placed on the intensifiers: 1) Flying leads, and 2) a transparent conductive coating on the fiber optic output window. Although all of the intensifiers could have been obtained with wraparound power

supplies in essentially the same mechanical envelope, we prefer to control the intensifier gain with digitally-controlled high voltage power supplies. The conductive coating isolates the CCD from any charge leakage caused by the high voltage (6000 V) on the intensifier anode.

Intensifiers from different manufacturers tend to have different dimensions, so a special external shell was needed to establish a common interface between the instrument and the CCD assembly. The housing is close fitting with potting cavities. A 50 mm x 50 mm format about the detector axis is maintained on three sides. Special attention was given to ensuring that the fiber optic window was plane with the back surface of the housing when the intensifier is potted into place. The flying leads were led through cavities to Reynolds 167-3770 connectors. The cavities were potted for insulation purposes.

Figure 15 illustrates the ICCD configuration. The fiber optic window is oil coupled to the face of the CCD. A ceramic frame is used to attach the window to the CCD package. This CCD assembly is then positioned in the larger housing with the window plane with the surface of the housing, since this is the interface to the intensifier. A small copper "evaporator" with copper inlet and outlet tubes is coupled to the rear of the CCD package for cooling. The contacts to the CCD pins are provided by constantan wire leading out the back. The cavity around the CCD pins is covered and the cavity is potted. The CCD housing and covers are Delrin, chosen for its electrical and thermal insulating properties. Two printed circuit boards are stacked on the back of the housing, one for CCD biasing and clocking and one for the pre-amplifier. A re-circulating Freon refrigeration system cools the CCD to its operating temperature, -20 C or lower. Although the AIS/SPAS instrument is radiatively cooled in space, cooling is required for laboratory operation and most ground based applications.

We have tried thermoelectric cooling of the CCD without much success. The heat load through the fiber optic window is large requiring high currents and therefore efficient heat sinking. This is not consistent with the small size that is desired.

The CCD read-out circuitry is enclosed in the electronics compartment below the spectrographs. Both the clocking and the analog signal line are shared among the CCD's. The electronics can control eight CCD's and intensifiers, as discussed below.

VI. Photometric Sensitivity

The sensitivity of both spectrographs and imagers was discussed in the companion paper Broadfoot and Sandel (1991) and will not be repeated here. This section deals with the technique of calibrating the instruments and results. Finally the results will be reconciled with the calculations to relate the design expectations to the instrument performance. The tools that were used in performing the instrument calibration include continuum light sources (quartz iodide lamps, hydrogen lamps), a set of calibrated passband filters, a detector which has been calibrated against a NBS standard detector, and a diffusing screen that filled the field of view of the spectrograph or imager being calibrated.

Two techniques were used in calibrating the spectrographs. The first approach was to illuminate the diffusing screen with the light source an bandpass filter. Filters were available for at least two wavelength regions within the spectral range of each spectrograph. The spectrum was recorded for each of the bandpass filters and the screen brightness was measured with the standard detector. The spectrograph record verified the transmission function of the filter. The integral of the recorded spectrum, compared to the brightness measured by the standard detector determined the instrument sensitivity at each filter wavelength. Second, the diffusing screen was illuminated by a stabilized continuum source. The continuum was recorded by all spectrographs simultaneously. The diffusing screen was observed by the standard detector through the bandpass filters to establish its brightness in specific wavelength bands. The spectrographic record established the run of intensity in the continuum. The comparison of the brightness measured through the bandpass filter with the recorded continuum spectrum established the sensitivity. The results of several calibrations are given

in Table 1 along with other parameters which are useful in comparing spectrographs. The sensitivity is reasonably constant through the spectral range of each spectrograph.

The second calibration method described above is the most useful for field work and for reconciling possible differences between spectrographs in their regions of overlap. The continuum intensity can be reproduced using regulated power supplies and confirmed by monitoring with a standard detector and single bandpass filter at a preferred wavelength.

Calibration of the imagers was straightforward. The continuum source was used to illuminate the screen and the continuum brightness was determined by the filters and standardized detector as described above. The sensitivity determined for each imager is given in Table 4, along with other characteristics of the imagers.

In the companion paper the expected sensitivity was calculated in terms of the Rayleigh-second, the emission rate in Rayleighs required to provide a signal-to-noise ratio of unity in one second. The calculation assumes that the ICCD detection system has photon counting efficiency and therefore the result is in photo events/sec resulting from an emission rate of 1 Rayleigh. The difference in the calculation and the measurement is in the gain of the system, the average signal level per photoevent can be calculated by combining the two measurements. If, for instance, a one Rayleigh emission rate produces 2.9 DN/sec and the sensitivity is 4 R-S. A single photoevent gives an average signal level of 11.6 DN.

VII. AIS Subsystems

The AIS subsystems include the sensor head with the spectrographs and imagers, the scan platform (SP), the instrument control unit (ICU), the low voltage power supplies (LVPS), the high voltage power supplies (HVPS), the data recording unit (DRU), the motor drive box (MDB), and interconnecting cabling. Table 5 lists the mass and dimensions of these subsystems. Figure 16 shows a block diagram of the subsystems and their interconnections.
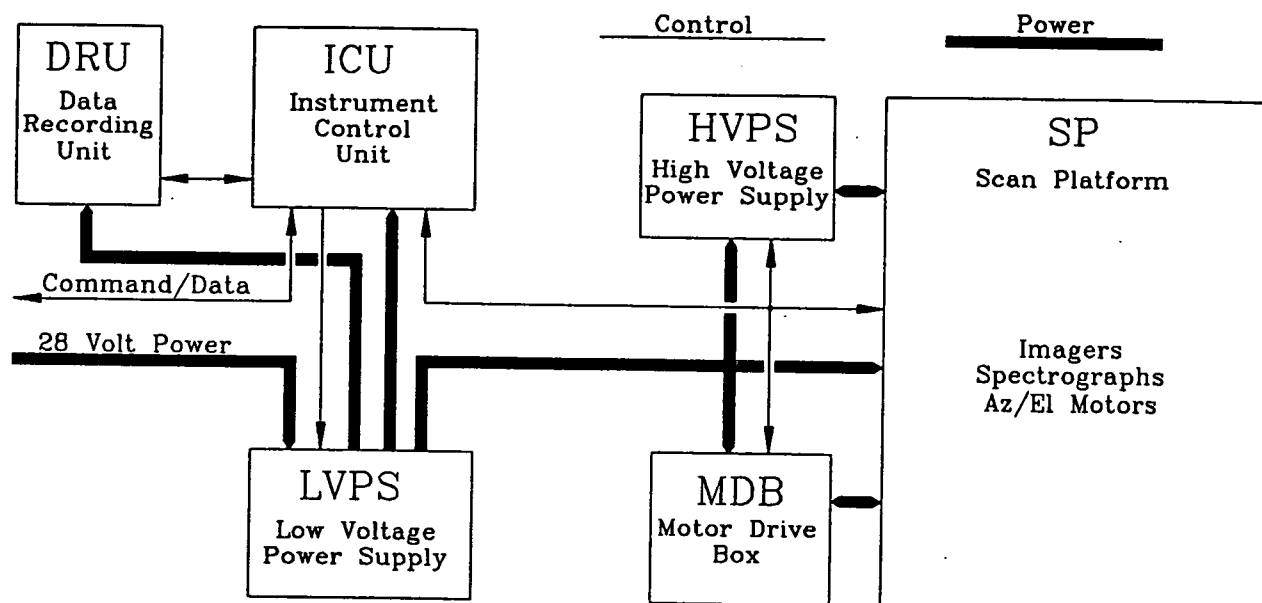
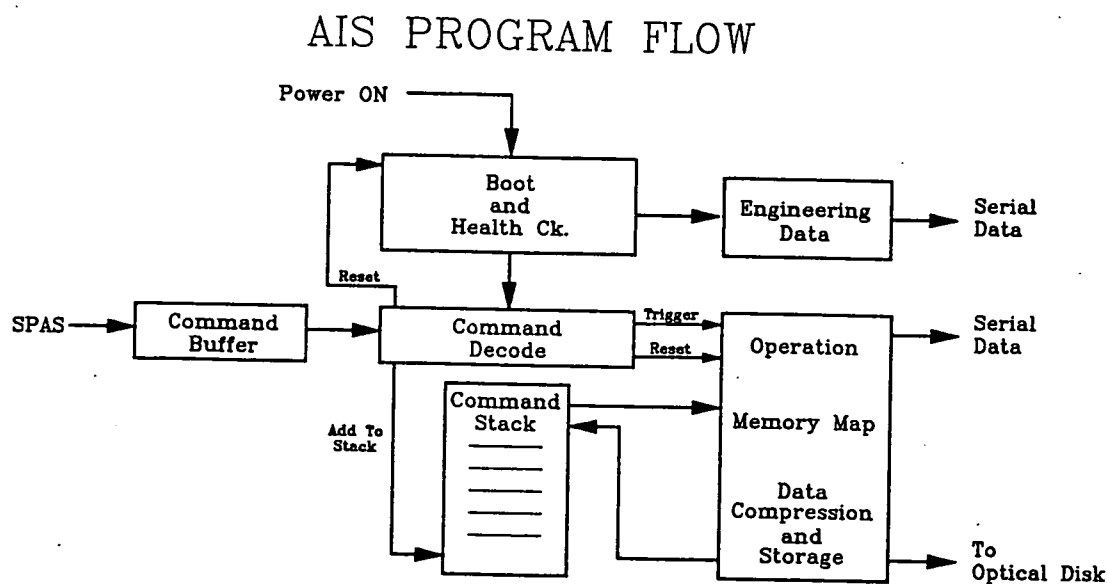Figure 16. Block diagram of the AIS electronics subsystems.

Figure 17. Logical blocks of the AIS control software.

Table 5. Mass and dimensions of AIS components.

AIS Component	Mass (kg)	Dimensions H x X x Y (cm)
SP	75	60 x 36 x 40
ICU	10	23 x 36 x 33
LVPS	8	10.5 x 35 x 26
HVPS	8	10 x 30 x 23
DRU	15	20 x 25 x 50
MDB	1	5.2 x 18 x 9.4
Cables	7	n/a

A. Scan Platform

A scan platform can direct the co-aligned fields of view of the AIS to specified targets. The platform has two axes of rotation, which we refer to as azimuth and elevation. The sensor head is suspended between two bearings on the elevations axis. This assembly is mounted on a turntable which provides the azimuth rotation. Both motions are driven by stepping motors through worm gears. For strength and reliability, the worm gears were doubly tapered cone gears manufactured by Cone Drive Textron which engage 19 teeth. The step size is 0.0082° in elevation and 0.014° in azimuth. The rotation range in elevation is -60° to 135° from the horizontal and in azimuth -175° to +175°. The scan rates are 105° per minute in azimuth and 52° per minute in elevation. The position is measured in terms of the number of steps from a fiducial microswitch for each axis.

B. Instrument Control Unit

All AIS functions are initiated in the computers housed in the ICU. This circuitry can be divided into three sections, the microcomputer, the CCD controller, and the interface circuitry. A VME backplane was used and all circuitry was fabricated on the double Eurocard printed circuit boards.

A CMOS single board computer controls the AIS. Important changes to provide reliability and flexibility were made in the memory addressable by the 80C86 microprocessor. The memory sections

are listed in Table 6. A custom "boot" program was written for the BIOS ROM. All of the essential startup and communications subroutines were included in the BIOS which was written into "Fused Link ROM" memory. The bit patterns in this memory cannot be altered permanently by high energy particle penetration. The operational programs for the AIS were written into EPROM but reliability was insured by providing three copies of the program and a load routine that would correct errors to the bit level.

Table 6 - Micro Computer Memory

Memory Type	Kbytes
"Boot" ROM (Fused Link)	8
Capacitor Backed-Up RAM	4K
EPROM	384
RAM	256
DATA RAM (Double Ported)	3000

Variable parameters are stored in capacitor-backed RAM so the instrument can be powered down without loss of information on the current instrument configuration. The AIS program is loaded from the EPROM to the RAM to run. A 3 megabyte double-ported memory serves for data accumulation and buffering.

Figure 17 is a diagram of program flow. When power is applied to the ICU the microcomputer performs the CPU health check, establishes the engineering telemetry link and completes the instrument functional tests. In flight, selected science data and engineering data will be cued for a real-time low rate data link. Most of the data is collected at high speed in the data memory, then transferred to an optical disk when the observation has been completed. Most of the

observing programs are stored in the EPROM because the command uplink capability in flight is very limited.

The CCD controller, referred to as the Micro Control Unit (MCU), contains a simple processor and memory. The readout format of the spectrographs (Figure 5) is selected by on-chip or off-chip summation to form effective pixels that are long and narrow by summing in the direction parallel to the slit. The effective pixel appears to be 1 x N real pixels long depending on the spatial resolution required. The imagers can be read out with on-chip or off-chip summation to form larger square pixels, 2x2, 3x3, etc. Pixel windows are addressable. High speed clocking is also available; the pixel shift rate can be increased from the 1 MHz rate used with digitization to a 4 MHz rate when charge is shifted but not digitized. Several read-out formats can be stored in the MCU program memory. Once a particular program is activated the MCU free runs.

C. Power Supplies and Data Recorder

The low voltage power supply subsystem contains 9 miniature power supplies and matching EMI filters manufactured by Integrated Circuit Inc. Turning on power to the AIS activates only the power supplies that power the ICU microprocessor. When the microprocessor has performed its self check, it can power other parts of the system as required. To save power and reduce heating, power supplies are turned on only when they are needed.

Each intensifier has its own high voltage power supply. The seven units were manufactured by K&M Electronics, Inc. (Model M2225). Digital inputs to each supply control the MCP voltage and photocathode gating potential.

Most of the data collected by the AIS will be stored on a 200 Mbyte WORM optical disk recorder manufactured by OptoTech and ruggedized to military specifications by Mountain Optech. The optical disk and its power converter are housed in a sealed vessel that maintains 1 atm pressure.

REFERENCES

Banks, P. M., P. R. Williamson, and W. J. Raitt, *Geophys. Res. Lett.*, **10**, 118 (1983).

Bernhardt, P. A., A Critical Comparison of Ionospheric Depletion Chemicals, *J. Geophys. Res.*, **92**, 4617 (1987).

Bernhardt, P. A., B. A. Kashiwa, C. A. Tepley, and S. T. Noble, Spacelab-2 Upper Atmospheric Modification Experiment Over Arecibo. 1. Neutral Gas Dynamics, *Astron. Lett. Commun.*, **27**, 169 (1988a).

Bernhardt, P. A., W. E. Swartz, M. C. Kelley, M. P. Sulzer, and S. T. Noble, Spacelab-2 Upper Atmospheric Modification Experiment Over Arecibo. 2. Plasma Dynamics, *Astron. Lett. Commun.*, **27**, 183 (1988b).

Broadfoot, A. L., and B. R. Sandel, Application of the ICCD to Airglow and Auroral Measurements, *this issue.*

Broadfoot, A. L., E. Anderson, P. Sherard, D. J. Knecht, R. A. Viereck, C. P. Pike, and E. Murad, Ground Optical Observations of Space Shuttle Firings at Varying Angles, *to be published.*

Mende, S. B., O. K. Garriott, and P. M. Banks, *Geophys. Res. Lett.*, **10**, 122 (1983).

Mendillo, M., J. Baumgartner, P. D. Allen, J. Foster, J. Holt, G. R. A. Ellis, A. Klekociuk and G. Reber, Spacelab-2 Plasma Depletion Experiments for Ionospheric and Radio Astronomical Studies, *Science*, **238**, 1260 (1987).

Murad, E., D. J. Knecht, R. A. Viereck, C. P. Pike, D. C. Cooke, I. L. Kofsky, C. A. Trowbridge, D. L. A. Rall, G. Ashley, L. Twist, J. B. Elgin, A. Setayesh, A. T. Stair, Jr., J. E. Blaha, Visible Light Emission Excited by Interaction of Space Shuttle Exhaust with the Atmosphere, *Geophys. Res. Lett.*, **17**, 2205 (1990).

Yau, A. W., B. A. Whalen, F. R. Harris, R. L. Gattinger, M. B. Pongratz, and P. A. Bernhardt, Simulations and Observations of Plasma Depletion, Ion Composition, and Airglow Emissions in Two Auroral Ionosphere Experiments, *J. Geophys. Res.*, **90**, 8387 (1985).